

Rigorous foundations of adaptive mode tracking in single-parametric Hermitian eigenvalue problems: existence theorems, error indicators, and application to SAFE dispersion analysis

Dong Xiao^{*} , Zahra Sharif-Khodaei , and M. H. Aliabadi 

Department of Aeronautics, Imperial College London, South Kensington, London SW7 2AZ, United Kingdom.

Abstract

The Semi-Analytical Finite Element (SAFE) method is widely used for computing guided wave dispersion curves in waveguides of arbitrary cross-section. Accurate mode tracking across consecutive wavenumber steps remains challenging, particularly in mode veering regions where eigenvalues become nearly degenerate and eigenvectors vary rapidly. This work establishes a rigorous theoretical framework for mode tracking in single-parameter Hermitian eigenvalue problems arising from SAFE formulations. We derive an explicit expression for the eigenvector derivative, revealing its inverse dependence on the eigenvalue gap, and prove that for any wavenumber and mode there exists a sufficiently small step ensuring unambiguous identification via the Modal Assurance Criterion. For symmetry-protected crossings, the Wigner–von Neumann non-crossing rule guarantees bounded eigenvector derivatives and reliable tracking even with coarse sampling. For continuous symmetries leading to degenerate subspaces, we introduce a rotation-invariant subspace MAC that treats each degenerate pair as a single entity. Based on these insights, we propose an adaptive wavenumber sampling algorithm that automatically refines the discretization where the MAC separation falls below a tolerance, using a novel error indicator to quantify tracking confidence. Validation on symmetric and unsymmetric laminates, an L-shaped bar, and a steel pipe demonstrates robust tracking in veering regions with substantially fewer points than uniform sampling or continuation-based approaches, while comparisons with open-source codes SAFEDC and Dispersion Calculator confirm accuracy and efficiency. The framework provides both theoretical guarantees and practical tools for reliable dispersion curve computation.

Keywords

Semi-Analytical Finite Element (SAFE); Dispersion curve tracing; Mode veering and crossing; Modal Assurance Criterion (MAC); Adaptive wavenumber sampling; A posteriori error estimation

^{0*}Corresponding author

¹Email addresses: d.xiao21@imperial.ac.uk (D. Xiao); z.sharif-khodaei@imperial.ac.uk (Z. Sharif-Khodaei); m.h.aliabadi@imperial.ac.uk (M.H. Aliabadi)

1 Introduction

Guided waves propagating in bounded structures exhibit strong dispersion and multimodal characteristics, playing a central role in ultrasonic nondestructive evaluation (NDE), structural health monitoring (SHM), and material characterization [1, 2]. Reliable dispersion analysis is a prerequisite for mode selection, signal interpretation, defect imaging, and inverse identification problems across diverse applications ranging from aerospace composites [3–5] to civil infrastructure [6] and biomedical imaging [7]. The accurate construction of dispersion curves—plots of frequency versus wavenumber or phase velocity—is therefore fundamental to both understanding wave physics and enabling practical inspection techniques.

A variety of numerical techniques have been developed to compute guided wave dispersion curves in waveguides of arbitrary cross-section and material complexity. The global matrix method (GMM) [8] represents one of the earliest systematic approaches, formulating the problem by assembling layer-specific matrices and searching for roots of the resulting determinant. While offering high accuracy for multilayered media, the GMM suffers from numerical instability at high frequency-thickness products due to exponential terms in the layer matrices. Transfer matrix methods (TMM) [9] provide a computationally more efficient alternative for layered waveguides by propagating fields from one interface to the next, but they may encounter exponential overflow issues in lossy or thick layers, limiting their practical applicability. Building upon these foundations, stiffness matrix methods (SMM) [10, 11] have been developed to combine the stability of global matrix approaches with the efficiency of recursive formulations for multilayered anisotropic media. The SMM constructs layer stiffness matrices and assembles them recursively, eliminating the need for explicit inversion of potentially ill-conditioned matrices. Parallel to these matrix-based approaches, spectral collocation techniques [12, 13] have emerged as powerful tools for smooth waveguides, achieving exponential convergence by expanding field variables in global basis functions such as Chebyshev or Legendre polynomials. More recently, wave finite element (WFE) methods [14] have gained prominence for periodic structures and phononic crystals, discretizing a single periodic segment and extracting dispersion relations through eigenvalue analysis of the resulting transfer matrix.

Among these techniques, the Semi-Analytical Finite Element (SAFE) method has emerged as one of the most widely adopted tools for guided wave dispersion analysis [15–17]. By discretizing the waveguide cross-section while assuming harmonic wave propagation along the axial direction, SAFE reduces the three-dimensional wave problem to a parameterized family of eigenvalue problems:

$$[\mathbf{K}(k) - \omega^2 \mathbf{M}] \mathbf{q} = \mathbf{0}, \quad (1)$$

where $\mathbf{K}(k) = \mathbf{K}_1 + ik\mathbf{K}_2 + k^2\mathbf{K}_3$ is a Hermitian matrix family depending on the wavenumber k for a lossless material with a traction-free boundary (the research scope of this paper focuses on the Hermitian system), \mathbf{M} is the real positive definite mass matrix, ω is the angular frequency, and \mathbf{q} is the eigenvector representing the cross-sectional displacement. The method offers computational efficiency and flexibility in modeling anisotropy, multilayered media, viscoelasticity, and complex cross-sections such as rails, pipelines, and L-shaped bars [18–20]. Recent developments have extended SAFE to piezoelectric materials [21], prestressed waveguides [22, 23], fluid-coupled configurations [17] and functionally graded materials [24].

The diversity of available numerical implementations has expanded considerably in recent years. Beyond established commercial software such as DISPERSE [25], open-source tools including the Dispersion Calculator (DC) [11, 26], SAFEDC [27], GUIGUW [28] and the Dispersion Box [29]

have democratized access to dispersion analysis capabilities. Each tool employs distinct numerical strategies—from root-finding methods like the stiffness matrix method in DC to eigenvalue-based approaches in SAFE implementations—offering complementary advantages in accuracy, speed, and robustness for different application scenarios.

Recent comparative studies have systematically evaluated the performance of these methods. Orta et al. [29] conducted a comprehensive benchmark of six commonly used techniques—including GMM, SMM, Hybrid Compliance-SMM (HCSMM), SAFE, Legendre Polynomial Method, and fifth-order shear deformation theory—for viscoelastic orthotropic multi-layer materials, providing quantitative insights into accuracy and computational efficiency across a wide frequency range. Similarly, Márquez and Rojas [30] evaluated five analytical and semi-analytical methods for Lamb wave dispersion in viscoelastic plates, demonstrating that the SAFE method achieves errors below 1% for fundamental modes while maintaining computational efficiency. Barazanchy and Giurgiutiu [31] further compared the unified analytic method, SAFE, and DISPERSE across isotropic and anisotropic laminates, offering guidance for method selection based on material complexity and accuracy requirements. These comparative studies collectively establish SAFE as a robust and accurate approach for guided wave dispersion analysis, particularly in multilayered anisotropic configurations.

Regardless of the underlying formulation, constructing continuous dispersion curves from discrete eigenvalue solutions requires a mode tracking or mode assignment procedure that consistently links eigenpairs across consecutive wavenumber or frequency steps. The Modal Assurance Criterion (MAC), introduced by Allemang and Brown [32], remains the most widely used similarity measure for this purpose due to its simplicity and computational efficiency [33]. When eigenvectors vary smoothly with the parameter, MAC-based tracking reliably preserves modal identities [34]. However, accurate mode tracking becomes fundamentally challenging in regions of strong modal interaction, particularly mode veering (also termed avoided crossing or osculation) [35, 36]. In veering regions, eigenvalues approach each other without intersecting while eigenvectors undergo rapid rotation over a narrow parameter interval [37, 38]. This phenomenon is generic in coupled Hermitian eigenvalue problems and arises whenever two modes belong to the same symmetry class [39]. The eigenvector derivative formula derived in this paper (Eq. (10)) reveals the underlying mechanism: the projection of the eigenvector derivative onto another mode is proportional to the coupling term $\mathbf{q}_j^H \mathbf{K}' \mathbf{q}_i$ and inversely proportional to the eigenvalue gap $\lambda_i - \lambda_j$. When the gap becomes small, the derivative becomes large, causing rapid eigenvector variation that can exceed the resolving capacity of a fixed parameter step. As a result, eigenvectors from different modes can become nearly indistinguishable over coarse steps [40], leading to frequent misassignments in veering regions.

The literature addressing mode tracking in dispersion analysis can be broadly categorized into two strands.

The first strand encompasses similarity-based methods, predominantly using MAC or related correlation measures to connect eigenpairs at adjacent steps [27, 41]. These approaches are straightforward to implement and perform well in regions where eigenvectors evolve slowly. However, their reliability degrades precisely in veering regions where they are most needed, as the rapid eigenvector variation can exceed the resolving capacity of fixed-step similarity measures [38]. The failure mode is characteristic: when the step size Δk exceeds the local critical step $\Delta k_{\max}(k)$, the correct mode may no longer yield the highest MAC value, causing the tracking algorithm to jump to a different branch.

The second strand comprises numerical continuation and trajectory-based methods, which track dispersion branches by enforcing smoothness, tangency, or curvature constraints [42]. By treating dispersion curves as continuous trajectories, these methods can navigate strong modal interactions. Continuation-based approaches underpin commercial software such as DISPERSE [25] and have been

implemented in open-source codes like the Dispersion Calculator (DC) [11, 26]. DC employs a mode-family division strategy that distinguishes Lamb, shear horizontal, and Scholte waves based on laminate symmetry and coupling properties, followed by a mode-by-mode extraction approach that independently traces each mode across a fixed frequency step [26]. While this method ensures robust tracking for well-separated modes, it inherits several limitations: it requires user-supplied initial guesses for each mode, the step size must be kept small to ensure corrector convergence (particularly in veering regions), the sequential nature of the algorithm limits parallel scalability, and the approach fundamentally relies on the non-singularity of the underlying Jacobian—a condition that fails precisely at symmetry-protected degeneracies.¹

Despite these advances, several key limitations persist across existing approaches. First, methods typically operate on uniform parameter grids, even though veering phenomena are highly localized. A grid fine enough to resolve the sharpest veering becomes prohibitively expensive when applied uniformly. Second, most approaches provide deterministic mode assignments without a quantitative confidence measure indicating when tracking may be unreliable. Veering regions are often either misclassified or oversmoothed, and intrinsically ambiguous intervals are not explicitly identified. Third, symmetry-protected degeneracy—where continuous symmetries force eigenvalues to coincide over entire intervals—poses a fundamental challenge to pointwise mode tracking. In such cases, eigenvectors are not uniquely defined within the degenerate subspace, causing conventional MAC-based methods to fail arbitrarily. These limitations are not unique to SAFE; they affect all dispersion formulations that require eigenpair sorting [43].

These limitations motivate the present work, which makes the following contributions:

1. **Rigorous perturbation analysis.** We derive an explicit expression for the eigenvector derivative in SAFE-based generalized eigenvalue problems (Section 2.3), establishing the inverse relationship between eigenvector sensitivity and eigenvalue gaps. This formula provides the mathematical foundation for understanding mode veering and the need for adaptive sampling.
2. **Symmetry protection analysis.** Using the Wigner–von Neumann non-crossing rule [36, 44, 45], we demonstrate that true crossings occur only when the coupling term vanishes identically, ensuring bounded eigenvector derivatives and reliable MAC-based tracking without special treatment (Section 2.5). For continuous symmetries leading to degeneracy, we introduce subspace MAC as a rotation-invariant similarity measure.
3. **Existence theorem for correct tracking.** We prove that in any mode veering region with positive eigengap, for every wavenumber k and mode i , there exists a step size $\Delta k_{\max}(k)$ such that the correct tracking condition $\text{MAC}[\mathbf{q}_i(k), \mathbf{q}_i(k + \Delta k)] > \text{MAC}[\mathbf{q}_i(k), \mathbf{q}_j(k + \Delta k)]$ holds for all $j \neq i$ (Section 2.6). This theorem guarantees that a sufficiently fine grid can always resolve modal transitions.
4. **Confidence-guided adaptive algorithm.** We propose an adaptive wavenumber sampling method that automatically refines the discretisation in regions where the MAC separation falls below a tolerance. A novel a posteriori error indicator $\varepsilon(k, \Delta k) = 1 - \min_i D_i(k, \Delta k)$ quantifies tracking confidence across all propagating modes (Section 2.8). The algorithm handles both non-degenerate modes and degenerate subspaces within a unified framework, detecting the latter on the fly and switching to subspace MAC.

¹The detailed implementation of DC’s tracing algorithm is not disclosed in the public literature; the description herein is based on the software’s observed behavior and official feature announcements [26].

5. **Comprehensive numerical validation.** The method is validated through five numerical examples spanning symmetric and unsymmetric laminated plates, L-shaped bars, and steel pipes, with comparisons against open-source codes SAFEDC [27] and the Dispersion Calculator [26] (Section 3). The results demonstrate superior mode tracking accuracy and efficiency, with adaptive grids using fewer points than uniform fine sampling while achieving perfect mode tracking. The steel pipe example specifically illustrates the handling of symmetry-protected degeneracy via subspace tracking.

The paper is organized as follows. Section 2 presents the SAFE formulation, MAC-based tracking, perturbation analysis, classification of modal interactions, symmetry protection proof, existence theorem, and adaptive algorithm. Section 3 provides numerical validations. Section 4 discusses the computational efficiency, compares continuation-based methods and frequency sweeping, and considers the role of the error indicator and handling symmetry-protected degeneracy. Section 5 summarizes the main conclusions, acknowledges limitations, and outlines directions for future work.

2 Methodology

2.1 Semi-Analytical Finite Element (SAFE)

The Semi-Analytical Finite Element (SAFE) method [15] provides an efficient computational framework for calculating dispersion characteristics in waveguides of uniform cross-section. This approach exploits the periodic nature of wave propagation along the axial direction while retaining the versatility of finite element discretization in the transverse plane.

For a waveguide extending infinitely in the x -direction with arbitrary cross-sectional geometry in the (y, z) -plane, the displacement field within an element can be expressed using a harmonic function along the propagation direction:

$$\mathbf{u}^{(e)}(x, y, z, t) = \mathbf{N}^{(e)}(y, z)\mathbf{q}^{(e)}e^{i(kx - \omega t)}, \quad (2)$$

where $\mathbf{N}^{(e)}(y, z)$ contains the shape functions and $\mathbf{q}^{(e)}$ is the vector of nodal displacements for the element. The parameters k and ω denote the wavenumber and angular frequency, respectively, and t is time. This representation takes advantage of the waveguide's translational symmetry, reducing the three-dimensional wave propagation problem to a two-dimensional analysis over the cross-section.

Substituting the assumed displacement form into the elastodynamic equations and applying the principle of virtual work leads to a quadratic eigenvalue problem in the wavenumber k :

$$(\mathbf{K}_1 + ik\mathbf{K}_2 + k^2\mathbf{K}_3 - \omega^2\mathbf{M})\mathbf{q} = \mathbf{0}, \quad (3)$$

where \mathbf{q} collects the nodal degrees of freedom of the entire cross-sectional discretization. The global matrices are assembled from element contributions:

$$\begin{aligned} \mathbf{K}_1 &= \int_A \mathbf{B}_0^T \mathbf{C} \mathbf{B}_0 dA, \\ \mathbf{K}_2 &= \int_A (\mathbf{B}_0^T \mathbf{C} \mathbf{B}_1 - \mathbf{B}_1^T \mathbf{C} \mathbf{B}_0) dA, \\ \mathbf{K}_3 &= \int_A \mathbf{B}_1^T \mathbf{C} \mathbf{B}_1 dA, \\ \mathbf{M} &= \int_A \rho \mathbf{N}^T \mathbf{N} dA. \end{aligned} \quad (4)$$

Here \mathbf{B}_0 and \mathbf{B}_1 are strain–displacement matrices associated with the zeroth and first derivatives with respect to x , \mathbf{C} is the material stiffness tensor (assumed real for lossless media), \mathbf{N} is the shape function matrix, ρ is the mass density, and A denotes the cross-sectional area. The matrices \mathbf{K}_1 , \mathbf{K}_2 and \mathbf{K}_3 represent, respectively, the stiffness contributions from cross-sectional deformation, coupling between axial and cross-sectional deformations, and axial deformation. \mathbf{M} is the consistent mass matrix. Under the assumption of lossless material with traction-free boundary conditions, \mathbf{C} is real, making \mathbf{K}_1 , \mathbf{K}_3 and \mathbf{M} symmetric, while \mathbf{K}_2 is skew-symmetric.

Two main strategies are commonly employed to extract dispersion curves from the SAFE formulation: wavenumber sweeping and frequency sweeping. In wavenumber sweeping, k is prescribed as a real parameter and the corresponding frequencies ω are obtained by solving the generalized eigenvalue problem

$$\mathbf{K}(k)\mathbf{q} = \lambda\mathbf{M}\mathbf{q}, \quad \lambda = \omega^2, \quad (5)$$

with $\mathbf{K}(k) = \mathbf{K}_1 + ik\mathbf{K}_2 + k^2\mathbf{K}_3$. This formulation is computationally attractive because it directly employs standard linear eigensolvers without the need for problem transformation. For any real k , $\mathbf{K}(k)$ is a complex Hermitian matrix ($\mathbf{K}(k) = \mathbf{K}^H(k)$), while \mathbf{M} is real, symmetric, positive definite and independent of k .

2.2 Mode tracking via the Modal Assurance Criterion (MAC)

2.2.1 Definition of MAC

The Modal Assurance Criterion (MAC) provides a measure of consistency between two eigenvectors [46]. For \mathbf{M} -orthonormal eigenvectors satisfying $\mathbf{q}_i^H \mathbf{M} \mathbf{q}_j = \delta_{ij}$, the MAC between $\mathbf{q}_i(k)$ and $\mathbf{q}_j(k + \Delta k)$ is defined as

$$\text{MAC}[\mathbf{q}_i(k), \mathbf{q}_j(k + \Delta k)] = |\mathbf{q}_i^H(k) \mathbf{M} \mathbf{q}_j(k + \Delta k)|^2. \quad (6)$$

The MAC takes values in $[0, 1]$, with values close to 1 indicating strong correlation and values near 0 indicating \mathbf{M} -orthogonality.

2.2.2 Correct tracking condition

At a given wavenumber k , we possess the eigenvector $\mathbf{q}_i(k)_{i=1}^M$ of mode i . After advancing to $k + \Delta k$, the full set of eigenvectors $\mathbf{q}_j(k + \Delta k)_{j=1}^N$ is computed. To establish correspondences between the two sets, we construct an $M \times N$ cost matrix \mathbf{C} with entries

$$C_{ij} = 1 - \text{MAC}[\mathbf{q}_i(k), \mathbf{q}_j(k + \Delta k)], \quad (7)$$

where the MAC is defined in Eq. (6). The Hungarian algorithm [47] is then applied to find the permutation σ that minimises the total cost $\sum_i C_{i,\sigma(i)}$, yielding the globally optimal one-to-one matching between modes at k and $k + \Delta k$.

A sufficient condition for this assignment to correctly identify every mode i (i.e., $\sigma(i) = i$ for all i) is that the self-MAC exceeds all cross-MAC values both row-wise and column-wise:

$$\begin{aligned} \text{MAC}[\mathbf{q}_i(k), \mathbf{q}_i(k + \Delta k)] &> \text{MAC}[\mathbf{q}_i(k), \mathbf{q}_j(k + \Delta k)] \quad \forall j \neq i, \\ \text{MAC}[\mathbf{q}_i(k), \mathbf{q}_i(k + \Delta k)] &> \text{MAC}[\mathbf{q}_j(k), \mathbf{q}_i(k + \Delta k)] \quad \forall j \neq i. \end{aligned} \quad (8)$$

The Eq. (8) contains both the row and column conditions. When Eq. (8) holds, each diagonal entry $C_{ii} = 1 - \text{MAC}[\mathbf{q}_i(k), \mathbf{q}_i(k + \Delta k)]$ is strictly smaller than every other entry in its row and column. It

imply that the identity permutation is the unique optimal assignment: any permutation that maps i to some $j \neq i$ would incur a cost larger than C_{ii} in either the row or the column constraint, and the sum of costs would exceed that of the identity permutation.

Therefore, the Hungarian algorithm must return the identity permutation, and every mode is correctly tracked. These conditions are sufficient but not necessary; in practice the Hungarian algorithm may still yield the correct matching even if they are violated, provided the global cost structure favours the identity. Nevertheless, row condition alone does not guarantee $\sigma(i) = i$ (especially when $M > N$), because a different permutation could still satisfy row minima if columns are not simultaneously minimal. Therefore, both row and column conditions are required for a rigorous sufficient criterion. These conditions underpins the MAC separation and error indicator developed in [Section 2.6](#), where we monitor the deviation from these conditions to detect intervals that require refinement.

2.3 Perturbation analysis of eigenvectors

Having introduced the MAC-based tracking condition, we now establish the essential perturbation results that quantify how eigenvectors change with the wavenumber k . These results are fundamental for understanding mode behaviour in both crossing and veering scenarios, and for proving the existence of a step size that guarantees correct tracking.

The analysis relies on the following standing assumption, which holds throughout this paper:

1. Analyticity: $\mathbf{K}(k)$ is analytic on $[k_{\min}, k_{\max}]$.
2. Simplicity: $\lambda_i(k) \neq \lambda_j(k)$ for all $i \neq j$ and all $k \in [k_{\min}, k_{\max}]$.

This ensures that the eigenvectors are uniquely defined up to a phase factor and vary analytically with k [48]. The phase ambiguity will be fixed later by a suitable normalization.

By differentiating the generalized eigenproblem $\mathbf{K}\mathbf{q}_i = \lambda_i\mathbf{M}\mathbf{q}_i$ with respect to k and projecting onto another eigenvector \mathbf{q}_j ($j \neq i$), we obtain the fundamental relation (detailed derivation provided in [Appendix A](#)):

$$\mathbf{q}_j^H \mathbf{M} \mathbf{q}'_i = \frac{\mathbf{q}_j^H \mathbf{K}' \mathbf{q}_i}{\lambda_i - \lambda_j}, \quad j \neq i. \quad (9)$$

This formula reveals that the projection of the eigenvector derivative onto another mode is proportional to the coupling term $\mathbf{q}_j^H \mathbf{K}' \mathbf{q}_i$ and inversely proportional to the eigenvalue gap $\lambda_i - \lambda_j$. The inverse dependence on the gap is the key to understanding why eigenvectors change rapidly in veering regions.

Expanding \mathbf{q}'_i in the \mathbf{M} -orthonormal eigenbasis and imposing a phase convention that eliminates the self-term ($\mathbf{q}_i^H \mathbf{M} \mathbf{q}'_i = 0$) yields the explicit expansion (see [Appendix A](#)):

$$\mathbf{q}'_i = \sum_{j \neq i} \frac{\mathbf{q}_j^H \mathbf{K}' \mathbf{q}_i}{\lambda_i - \lambda_j} \mathbf{q}_j. \quad (10)$$

[Eq. \(10\)](#) is the cornerstone of our analysis. It shows that the sensitivity of an eigenvector is governed by two factors: the coupling strength between modes (numerator) and the eigenvalue gap (denominator). When the gap becomes small, the corresponding term in the sum becomes large, signalling rapid variation of the eigenvector.

Finally, the \mathbf{M} -norm of the derivative provides a quantitative measure of this sensitivity:

$$\|\mathbf{q}'_i\|_{\mathbf{M}}^2 = \sum_{j \neq i} \frac{|\mathbf{q}_j^H \mathbf{K}' \mathbf{q}_i|^2}{(\lambda_i - \lambda_j)^2}, \quad (11)$$

where $\|\mathbf{v}\|_{\mathbf{M}}^2 := \mathbf{v}^H \mathbf{M} \mathbf{v}$. This quantity is well-defined because each denominator is non-zero under the simplicity assumption. With these perturbation results established, we now proceed to classify the different scenarios that arise in SAFE dispersion curves.

2.4 Challenges in SAFE mode tracking

While the MAC offers a simple and effective tool for mode tracking, its success critically depends on the behaviour of eigenvectors as k varies. In SAFE dispersion analysis, three phenomena can jeopardise the tracking: mode crossing, mode veering, and mode degeneracy. To understand their influence, it is instructive to examine a reduced two-degree-of-freedom model that captures the essential interaction between two nearly coincident modes.

2.4.1 A two-state local approximation

Consider the projection of the eigenproblem Eq. (5) onto the subspace spanned by two eigenvectors $\mathbf{q}_i(k_0)$ and $\mathbf{q}_j(k_0)$ at a reference wavenumber k_0 where the corresponding eigenvalues $\lambda_i(k_0) = \omega_i^2(k_0)$ and $\lambda_j(k_0) = \omega_j^2(k_0)$ are close. For k near k_0 , the effective 2×2 Hermitian matrix reads

$$\mathbf{H}(k) = \begin{pmatrix} a(k) & b(k) \\ b^*(k) & c(k) \end{pmatrix}, \quad (12)$$

with $a(k), c(k) \in \mathbb{R}$ and $b(k) \in \mathbb{C}$. The diagonal entries are $a(k) = \mathbf{q}_i^H(k_0) \mathbf{K}(k) \mathbf{q}_i(k_0)$ and $c(k) = \mathbf{q}_j^H(k_0) \mathbf{K}(k) \mathbf{q}_j(k_0)$, while the off-diagonal term $b(k) = \mathbf{q}_i^H(k_0) \mathbf{K}(k) \mathbf{q}_j(k_0)$ quantifies the coupling between the two modes. Its derivative at k_0 , $b'(k_0) = \mathbf{q}_i^H(k_0) \mathbf{K}'(k_0) \mathbf{q}_j(k_0)$, is precisely the coupling coefficient that appears in the eigenvector derivative formula Eq. (9) derived in Section 2.3. The two eigenvalues of $\mathbf{H}(k)$ are

$$\lambda_{\pm}(k) = \frac{a(k) + c(k)}{2} \pm \frac{1}{2} \sqrt{|a(k) - c(k)|^2 + 4|b(k)|^2}. \quad (13)$$

2.4.2 Four scenarios and their implications for MAC tracking

Building upon the two-state local approximation introduced in Eq. (13), we now systematically classify the possible interactions between two modes in a single-parameter Hermitian eigenproblem, summarise them in Table 1 and discuss each in turn.

Scenario 1 – Symmetry-protected true crossing. If the two modes belong to different irreducible representations of a symmetry respected by the waveguide, the off-diagonal coupling vanishes identically: $b(k) \equiv 0$ for all k . The eigenvalues are simply $a(k)$ and $c(k)$, and a true crossing occurs when $a(k) = c(k)$. Because $b(k) = 0$, the eigenvectors do not mix; they remain the uncoupled ones and vary analytically through the crossing. Consequently, the MAC condition Eq. (8) holds even for relatively coarse steps – this is the benign situation analysed in Section 2.5.

Scenario 2 – Avoided crossing (veering). In the absence of symmetry, $b(k) \neq 0$ generically. The eigenvalues cannot become exactly equal (the square-root term never vanishes); instead they approach each other, reach a minimum separation (the gap), and then diverge – a phenomenon known

Table 1: Four scenarios characterising the interaction between two modes in a single-parameter Hermitian eigenproblem and their impact on MAC tracing.

Scenario	Eigenvalue relation	Coupling $ b(k) $	Eigenvector behaviour	MAC tracking
True crossing (symmetry-protected)	$\lambda_i = \lambda_j$ at isolated k	$\equiv 0$	Modes remain distinct; eigenvectors vary smoothly	Easy
Avoided crossing (generic veering)	$\lambda_i \approx \lambda_j$ (gap > 0)	> 0	Rapid, continuous exchange over a narrow k interval	Demands small Δk
Crossing with non-zero coupling		Impossible in single-parameter Hermitian systems		
Symmetry-protected degeneracy	$\lambda_i = \lambda_j$ (all k)	$\equiv 0$	Subspace invariant, vector rotates arbitrarily in subspace	Pointwise MAC invalid (subspace tracing required)

as avoided crossing or veering. Over the narrow k interval where the gap is small, the eigenvectors undergo a rapid but continuous exchange. The derivative formula Eq. (10) shows that the eigenvector sensitivity is inversely proportional to the eigenvalue gap; hence in veering regions the eigenvectors change dramatically. MAC tracking then requires a step size Δk small enough to resolve this variation. Theorem 1 in Section 2.6 guarantees that such a sufficiently small Δk always exists, and the adaptive algorithm (Section 2.8) automatically supplies it.

Scenario 3 – Crossing with non-zero coupling (impossible). For a single-parameter Hermitian matrix family, a true eigenvalue crossing ($\lambda_i = \lambda_j$) necessarily forces $b(k) = 0$. This is a direct consequence of the Wigner–von Neumann non-crossing rule (Section 2.5.1). Hence the combination “crossing + non-zero coupling” cannot occur; it is listed only for logical completeness.

Scenario 4 – Symmetry-protected degeneracy (SPD). When the waveguide possesses a continuous symmetry (e.g., axisymmetry in a pipe), modes may form degenerate pairs – such as the $\sin(m\theta)$ and $\cos(m\theta)$ modes in a circular cylinder – with identical eigenvalues across the entire wavenumber range. In this case $b(k) \equiv 0$ and $a(k) = c(k)$ for all k , so the two eigenvalues coincide globally. The eigenvectors are not uniquely defined within the two-dimensional invariant subspace; any orthonormal basis of this subspace is equally valid. While the eigenvalue gap is zero, the coupling term also vanishes, so the eigenvector derivative formula Eq. (10) remains bounded. However, pointwise MAC tracking between adjacent k steps becomes ill-posed because the computed eigenvectors may undergo arbitrary rotations within the subspace due to small numerical perturbations. This symmetry-protected degeneracy requires a different treatment: instead of tracking individual modes, one must track the subspace they span. The stability of the subspace itself can vary with k ; our numerical experiments on a steel pipe (Section 3.4) show that the subspace rotation may be significant at low wavenumbers but negligible at high wavenumbers. Consequently, the adaptive algorithm can be extended to monitor a subspace similarity measure and refine the grid where the subspace changes rapidly. The extension to degenerate subspaces is discussed in Section 2.7.

These four scenarios capture the essential behaviour of mode interactions in SAFE dispersion curves. The next subsections will provide rigorous mathematical backing for the observations summarised here, culminating in an adaptive algorithm that guarantees correct tracking regardless of whether the situation is a symmetry-protected crossing or a strongly veering avoided crossing.

2.5 Why genuine crossings are benign: symmetry protection

This subsection focuses on symmetry-protected crossings, i.e., isolated parameter values where two distinct modes belonging to different symmetry classes become coincident. While [Section 2.4](#) qualitatively identified symmetry-protected crossings as benign for MAC-based tracking, this subsection provides the rigorous mathematical justification. We demonstrate that when a true crossing occurs in a single-parameter Hermitian eigenproblem, it must be accompanied by a vanishing coupling term, which in turn guarantees bounded eigenvector derivatives and smooth variation through the crossing. Consequently, the correct tracking condition [Eq. \(8\)](#) holds even for relatively coarse wavenumber steps.

2.5.1 The Wigner–von Neumann non-crossing rule

The fundamental obstruction to arbitrary crossings is encapsulated in the Wigner–von Neumann non-crossing rule [[36](#), [44](#), [45](#)]. For a Hermitian matrix family $\mathbf{H}(p)$ depending analytically on a single real parameter p , eigenvalues corresponding to states of the same symmetry cannot cross; instead they repel each other, producing an avoided crossing. A true crossing can occur only if the two states belong to different symmetry classes of a symmetry respected by $\mathbf{H}(p)$ for all p . In such a case, the off-diagonal matrix element coupling the two states is identically zero.

In the SAFE context, where $\mathbf{K}(k)$ is Hermitian, a crossing $\lambda_i(k_0) = \lambda_j(k_0)$ ($i \neq j$) is possible only if

$$\mathbf{q}_j^H(k_0)\mathbf{K}'(k_0)\mathbf{q}_i(k_0) = 0. \quad (14)$$

Moreover, because the symmetry is present for all k , the coupling vanishes identically in a neighbourhood of k_0 , i.e. $\mathbf{q}_j^H(k)\mathbf{K}'(k)\mathbf{q}_i(k) \equiv 0$ for k near k_0 .

2.5.2 Implication for eigenvector derivatives

Recall the eigenvector derivative expansion derived in [Section 2.3](#) ([Eq. \(10\)](#)):

$$\mathbf{q}'_i(k) = \sum_{m \neq i} \frac{\mathbf{q}_m^H(k)\mathbf{K}'(k)\mathbf{q}_i(k)}{\lambda_i(k) - \lambda_m(k)} \mathbf{q}_m(k). \quad (15)$$

For a crossing between modes i and j at k_0 , we have $\lambda_i(k_0) = \lambda_j(k_0)$. The term $m = j$ in the sum would appear to have a vanishing denominator, potentially causing a singularity. However, condition [Eq. \(14\)](#) ensures that the numerator also vanishes at k_0 ; in fact, because the coupling is identically zero near k_0 , the ratio $\frac{\mathbf{q}_j^H\mathbf{K}'\mathbf{q}_i}{\lambda_i - \lambda_j}$ remains bounded and, by analyticity, extends to a well-defined limit at k_0 . All other terms in the sum are regular because $\lambda_i - \lambda_m \neq 0$ for $m \neq i, j$. Consequently, $\mathbf{q}'_i(k)$ is bounded and continuous through the crossing.

2.5.3 Smooth eigenvector variation and MAC tractability

A bounded derivative implies Lipschitz continuity of the eigenvector: there exists a constant $L_i > 0$ such that for sufficiently small Δk ,

$$\|\mathbf{q}_i(k + \Delta k) - \mathbf{q}_i(k)\|_{\mathbf{M}} \leq L_i. \quad (16)$$

This smoothness guarantees that the self-MAC $\text{MAC}[\mathbf{q}_i(k), \mathbf{q}_i(k + \Delta k)]$ remains close to 1 even for relatively large steps, while the cross-MAC with any other mode $j \neq i$ remains small (of order $|\Delta k|^2$).

Hence the correct tracking condition [Eq. \(8\)](#) is satisfied for all Δk up to some finite value determined by the local curvature – no exotic step-size restriction is needed.

In contrast, for an avoided crossing (Scenario 2), the coupling is non-zero, the eigenvalue gap becomes small, and the denominator in [Eq. \(15\)](#) makes \mathbf{q}'_i large. Then a sufficiently small Δk is essential – a situation addressed in [Section 2.6](#).

Thus, symmetry-protected genuine crossings are benign: they do not challenge MAC-based tracking and can be safely traversed with the initial coarse grid. This understanding completes our classification and sets the stage for the adaptive algorithm that deals with the genuinely difficult case of veering.

Remark. The situation is fundamentally different when the symmetry forces eigenvalues to coincide over an entire interval – a phenomenon known as symmetry-protected degeneracy. In that case, while the coupling also vanishes, the eigenvectors are not uniquely defined within the degenerate subspace. Pointwise MAC tracking becomes ill-posed and must be replaced by subspace tracking, which will be discussed in [Section 2.7](#).

2.6 Overcoming avoided crossings: existence of a sufficiently small step

Having established that symmetry-protected crossings pose no difficulty for MAC-based tracking, we now turn to the more challenging scenario of avoided crossings (veering). In such regions, the eigenvalue gap $\lambda_i - \lambda_j$ becomes small while the coupling $\mathbf{q}_j^H \mathbf{K}' \mathbf{q}_i$ remains non-zero. [Eq. \(10\)](#) then predicts a large eigenvector derivative, implying rapid variation of the mode shape over a short k -interval. Consequently, the success of MAC tracking hinges on using a step size Δk that is sufficiently small to resolve this variation.

In this subsection, we prove that, under the same regularity assumptions as before, such a sufficiently small step always exists. More precisely, we show that for every wavenumber k and every mode i , there exists a positive number $\Delta k_{\max}(k)$ such that for any $0 < \Delta k \leq \Delta k_{\max}(k)$ the following inequality holds:

$$\text{MAC}[\mathbf{q}_i(k), \mathbf{q}_i(k + \Delta k)] > \text{MAC}[\mathbf{q}_i(k), \mathbf{q}_j(k + \Delta k)] \quad \forall j \neq i, \quad (17)$$

even in the most severe veering regions. This is precisely the row-wise condition in [Eq. \(8\)](#) introduced in [Section 2.2](#). The corresponding column-wise condition,

$$\text{MAC}[\mathbf{q}_i(k), \mathbf{q}_i(k + \Delta k)] > \text{MAC}[\mathbf{q}_j(k), \mathbf{q}_i(k + \Delta k)] \quad \forall j \neq i, \quad (18)$$

follows directly from the same result by considering the interval $[k, k + \Delta k]$ in the reverse direction. Specifically, [Eq. \(17\)](#) guarantees correct forward tracking from k to $k + \Delta k$, while applying the same reasoning to the interval $[k + \Delta k, k]$ yields the backward tracking condition [Eq. \(18\)](#). Therefore, we focus on proving [Eq. \(17\)](#) in this subsection.

2.6.1 Theorem statement

Theorem 1 (Local Correct Tracking). Consider the single-parameter Hermitian eigenvalue problem $[\mathbf{K}(k) - \lambda \mathbf{M}] \mathbf{q} = \mathbf{0}$, defined for $k \in [k_{\min}, k_{\max}]$. Assume that:

- (i) $\mathbf{K}(k)$ is Hermitian for all k and analytic on $[k_{\min}, k_{\max}]$;
- (ii) \mathbf{M} is a constant, real positive definite matrix;

- (iii) the eigenvalues are simple throughout the interval, i.e., $\lambda_i(k) \neq \lambda_j(k)$ for all distinct indices i, j and all $k \in [k_{\min}, k_{\max}]$.

Then, for every $k \in [k_{\min}, k_{\max})$ and every mode index i , there exists a positive number $\Delta k_{\max}(k) > 0$ such that for all $0 < \Delta k \leq \Delta k_{\max}(k)$,

$$\text{MAC}[\mathbf{q}_i(k), \mathbf{q}_i(k + \Delta k)] > \text{MAC}[\mathbf{q}_i(k), \mathbf{q}_j(k + \Delta k)], \quad \forall j \neq i. \quad (19)$$

Remark 1. Condition (iii) excludes the case of symmetry-protected degeneracy, where eigenvalues coincide over an interval. For isolated symmetry-protected crossings (where $\lambda_i = \lambda_j$ at a point but the coupling vanishes), the conclusion of the theorem remains valid by continuity, as the eigenvector derivative remains bounded and the MAC inequality holds in the limit.

Remark 2. The admissible step bound $\Delta k_{\max}(k)$ depends on the local spectral properties—specifically on the size of the eigenvalue gaps and the coupling strengths at k . In veering regions where gaps are tiny, $\Delta k_{\max}(k)$ becomes correspondingly small, reflecting the need for finer sampling.

Proof Sketch: The complete proof of Theorem 1 is provided in [Appendix B](#). Here we outline the essential ideas. Using the analyticity of the eigenvectors, we expand $\mathbf{q}_i(k + \Delta k)$ in a Taylor series around k . Employing the phase condition [Eq. \(35\)](#) and the projection formula [Eq. \(9\)](#), we obtain the asymptotic expansions:

$$\begin{aligned} \text{MAC}[\mathbf{q}_i(k), \mathbf{q}_i(k + \Delta k)] &= 1 - (\Delta k)^2 \|\mathbf{q}'_i(k)\|_{\mathbf{M}}^2 + O((\Delta k)^3), \\ \text{MAC}[\mathbf{q}_i(k), \mathbf{q}_j(k + \Delta k)] &= (\Delta k)^2 |c_{ij}(k)|^2 + O((\Delta k)^3), \end{aligned} \quad (20)$$

where $c_{ij}(k) = \frac{\mathbf{q}_i^H(k) \mathbf{K}'(k) \mathbf{q}_j(k)}{\lambda_j(k) - \lambda_i(k)}$ is bounded. From these asymptotic forms, one can choose constants C_1, C_2 and a $\delta_0 > 0$ such that for all $0 < \Delta k \leq \delta_0$,

$$\begin{aligned} \text{MAC}[\mathbf{q}_i(k), \mathbf{q}_i(k + \Delta k)] &\geq 1 - C_1(\Delta k)^2, \\ \text{MAC}[\mathbf{q}_i(k), \mathbf{q}_j(k + \Delta k)] &\leq C_2(\Delta k)^2. \end{aligned} \quad (21)$$

Setting $\Delta k_{\max}(k) = \min(\delta_0, 1/\sqrt{C_1 + C_2})$ guarantees that $1 - C_1(\Delta k)^2 > C_2(\Delta k)^2$, thereby establishing the desired inequality. The detailed construction of these constants and the rigorous control of higher-order terms are given in [Appendix B](#).

2.6.2 Corollary: positive MAC separation

Define the MAC separation for mode i as

$$\begin{aligned} D_i(k, \Delta k) &:= \min(D_i^{\text{row}}(k, \Delta k), D_i^{\text{col}}(k, \Delta k)), \\ D_i^{\text{row}}(k, \Delta k) &= \text{MAC}[\mathbf{q}_i(k), \mathbf{q}_i(k + \Delta k)] - \max_{j \neq i} \text{MAC}[\mathbf{q}_i(k), \mathbf{q}_j(k + \Delta k)], \\ D_i^{\text{col}}(k, \Delta k) &= \text{MAC}[\mathbf{q}_i(k), \mathbf{q}_i(k + \Delta k)] - \max_{j \neq i} \text{MAC}[\mathbf{q}_j(k), \mathbf{q}_i(k + \Delta k)]. \end{aligned} \quad (22)$$

Theorem 1 guarantees that there exists positive value of $\Delta k_{\max}(k)$, such that for all $0 < \Delta k \leq \Delta k_{\max}(k)$, we have $D_i^{\text{row}}(k, \Delta k) > 0$ and $D_i^{\text{col}}(k, \Delta k) > 0$. The magnitude of D_i reflects the confidence of the mode identification: a larger value indicates a clearer distinction between the correct mode and the closest competing mode. Conversely, a small (or negative) D_i signals that the current step Δk exceeds the local critical step size, potentially causing mode misidentification. Hence D_i can serve as a reliability indicator for mode i over the interval $[k, k + \Delta k]$.

To obtain a single scalar measure for the entire interval that accounts for all propagating modes, we define the a posteriori error indicator for mode tracking as

$$\varepsilon(k, \Delta k) = 1 - \min_i D_i(k, \Delta k). \quad (23)$$

Since $-1 \leq D_i(k, \Delta k) \leq 1$, we have $\varepsilon(k, \Delta k) \in [0, 2]$. A value of ε close to 0 implies that every mode is tracked with high confidence (all D_i are near 1), whereas a value near 1 indicates that at least one mode is at risk of being misidentified ($\min_i D_i$ small or negative). This error indicator will be used in the adaptive algorithm to decide where refinement is needed.

2.7 Symmetry-protected degeneracy: subspace tracking

When the waveguide possesses a continuous symmetry (e.g., axisymmetry in a pipe), eigenvalues may become degenerate over entire intervals. The most common example is the pair of $\sin(m\theta)$ and $\cos(m\theta)$ modes in a circular cylinder, which share the same eigenvalue for all wavenumbers k . In such cases, the coupling term $\mathbf{q}_j^H \mathbf{K}' \mathbf{q}_i$ vanishes identically due to symmetry, but the eigenvectors are not uniquely defined: any orthonormal basis of the two-dimensional invariant subspace is equally valid. Consequently, pointwise MAC tracking between adjacent wavenumber steps is ill-posed – the numerically computed eigenvectors may undergo arbitrary rotations within the subspace, causing the MAC to fluctuate unpredictably even when the subspace itself evolves smoothly.

2.7.1 Detecting degeneracy

In practice, degeneracy can be detected by examining the eigenvalue spectrum: if $|\lambda_i(k) - \lambda_j(k)| < \varepsilon_{\text{eig}}$ and the off-diagonal coupling $|\mathbf{q}_i^H \mathbf{K}'(k) \mathbf{q}_j|$ is also below a threshold (indicating symmetry protection), the two modes are considered degenerate. For SAFE formulations with axisymmetric cross-sections, such pairs can also be identified a priori by their circumferential order m .

2.7.2 Subspace similarity measures

To track the evolution of a degenerate subspace, we require a measure that compares two subspaces rather than individual vectors. Let $\mathbf{Q}(k)$ and $\mathbf{Q}(k + \Delta k)$ be $n \times d$ matrices whose columns form \mathbf{M} -orthonormal bases of the d -dimensional degenerate subspace at the two wavenumbers, i.e., $\mathbf{Q}^H(k) \mathbf{M} \mathbf{Q}(k) = \mathbf{I}_d$ and similarly for $k + \Delta k$. A natural extension of the MAC to subspaces is the subspace MAC defined as

$$\text{MAC}_{\text{sub}}[\mathbf{Q}(k), \mathbf{Q}(k + \Delta k)] = \frac{1}{d} |\mathbf{Q}^H(k) \mathbf{M} \mathbf{Q}(k + \Delta k)|_F^2, \quad (24)$$

where $|\cdot|_F$ denotes the Frobenius norm. This quantity ranges between 0 and 1, attaining 1 when the two subspaces coincide (i.e., their columns span the same space) and 0 when they are \mathbf{M} -orthogonal. For a one-dimensional subspace ($d = 1$), \mathbf{Q} reduces to a single vector \mathbf{q} , and the subspace MAC collapses to the standard vector MAC (Eq. (6)). Thus the subspace MAC provides a unified similarity measure applicable to both non-degenerate modes and degenerate subspaces.

Remark. Other metrics exist for comparing subspaces, such as the largest principal angle θ_{max} , whose cosine is the smallest singular value of $\mathbf{Q}^H(k) \mathbf{M} \mathbf{Q}(k + \Delta k)$. While geometrically intuitive, the subspace MAC is preferred here because it directly generalises the familiar MAC and fits seamlessly into the adaptive framework introduced in next [Section 2.8](#).

2.7.3 Adaptive subspace refinement

With the subspace MAC defined, each degenerate subspace can be treated analogously to a single mode in the adaptive procedure. Consider an interval $[k_p, k_{p+1}]$. Let $\mathcal{S}p$ denote a degenerate subspace (of dimension d) at k_p , and $\mathcal{S}p + 1$ the corresponding subspace at k_{p+1} (obtained, for instance, by identifying eigenvalue clusters). We compute the subspace MAC between them:

$$\text{MAC}_{\text{sub}}[\mathbf{Q}\mathcal{S}p(k_p), \mathbf{Q}\mathcal{S}p + 1(k_{p+1})], \quad (25)$$

where $\mathbf{Q}\mathcal{S}p(k_p)$ and $\mathbf{Q}\mathcal{S}p + 1(k_{p+1})$ are orthonormal bases for the two subspaces. Because the subspace MAC satisfies the same properties as the vector MAC, we can directly apply the definitions of [Section 2.6.2](#). For each “object” (whether a single mode or a subspace), we define its MAC separation as

$$\begin{aligned} D_{\mathcal{S}}(k_p, \Delta k_p) &= \min(D_{\mathcal{S}}^{\text{row}}(k_p, \Delta k_p), D_{\mathcal{S}}^{\text{col}}(k_p, \Delta k_p)), \\ D_{\mathcal{S}}^{\text{row}}(k_p, \Delta k_p) &= \text{MAC}_{\text{sub}}[\mathbf{Q}\mathcal{S}(k_p), \mathbf{Q}\mathcal{S}(k_{p+1})] - \max_{\mathcal{T} \neq \mathcal{S}} \text{MAC}_{\text{sub}}[\mathbf{Q}\mathcal{S}(k_p), \mathbf{Q}\mathcal{T}(k_{p+1})], \\ D_{\mathcal{S}}^{\text{col}}(k_p, \Delta k_p) &= \text{MAC}_{\text{sub}}[\mathbf{Q}\mathcal{S}(k_p), \mathbf{Q}\mathcal{S}(k_{p+1})] - \max_{\mathcal{T} \neq \mathcal{S}} \text{MAC}_{\text{sub}}[\mathbf{Q}\mathcal{T}(k_p), \mathbf{Q}\mathcal{S}(k_{p+1})], \end{aligned} \quad (26)$$

where the maximum is taken over all other objects (other modes or subspaces) at k_{p+1} . The overall error indicator for the interval is then

$$\varepsilon(k_p, \Delta k_p) = 1 - \min_{\mathcal{S}} D_{\mathcal{S}}(k_p, \Delta k_p), \quad (27)$$

exactly as in [Eq. \(23\)](#). If $\varepsilon(k_p, \Delta k_p) > \bar{\varepsilon}$ and $\Delta k_p > \Delta k_{\min}$, the interval is marked for refinement. The refinement process proceeds identically to the non-degenerate case.

This unified treatment ensures that the adaptive algorithm automatically handles symmetry-protected degeneracy without any modification to its core logic. The only additional requirement is the identification of degenerate subspaces at each wavenumber, which can be done by clustering eigenvalues that are equal (within tolerance) and whose corresponding eigenvectors are decoupled (coupling term negligible). In the steel pipe example ([Section 3.4](#)), we demonstrate how this approach correctly resolves the evolution of degenerate mode pairs.

2.8 Adaptive wavenumber sampling algorithm

The theoretical analysis of [Section 2.6](#) guarantees that for every wavenumber k and mode i there exists a step size $\Delta k_{\max}(k)$ such that the correct tracking condition [Eq. \(19\)](#) holds. However, $\Delta k_{\max}(k)$ is unknown a priori and varies strongly along the dispersion curve—it becomes extremely small in veering regions where eigenvalue gaps are tiny. A uniform sampling strategy would therefore be either inefficient (if a very fine step is used everywhere) or inaccurate (if the step is too coarse in veering regions). To overcome this dilemma, we propose an adaptive wavenumber sampling algorithm that automatically refines the discretization in regions where the error indicator $\varepsilon(k, \Delta k)$ (defined in [Eq. \(23\)](#)) exceeds a prescribed tolerance. The algorithm is summarised in the flowchart of [Fig. 1](#).

2.8.1 Algorithm description

The algorithm proceeds as follows (refer to [Fig. 1](#)):

1. **Initialization.** Set the wavenumber range $[k_{\min}, k_{\max}]$, the maximum phase velocity v_p^{\max} (used to determine the frequency range), the error tolerance $\bar{\varepsilon}$, the minimum allowed step size

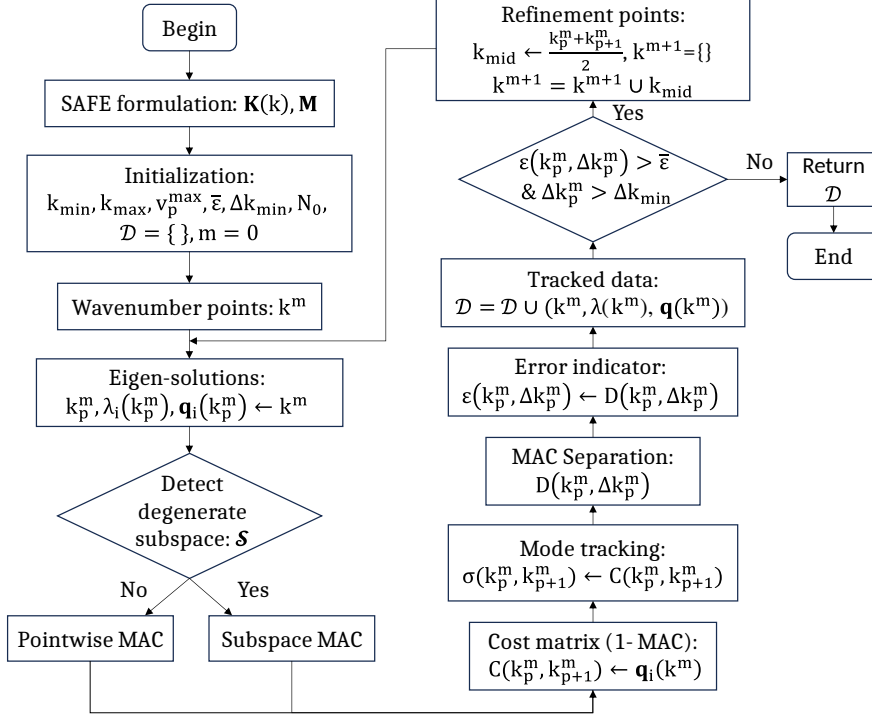


Figure 1: Flowchart of the adaptive wavenumber sampling algorithm. The process iteratively solves eigenvalue problems, computes error indicators, and refines the grid where the error exceeds the tolerance.

Δk_{\min} , the initial number of grid points N_0 , and the iteration counter $m = 0$. The initial grid $k^{m=0} = [k_1^{(0)}, \dots, k_{N_0}^{(0)}]$ is uniformly spaced.

2. **Solve eigenvalue problems in parallel.** At each wavenumber $k_p^{(m)}$ in the current grid, solve the generalized eigenproblem $\mathbf{K}(k)\mathbf{q} = \lambda\mathbf{M}\mathbf{q}$ to obtain all eigenpairs $(\lambda_i(k_p^{(m)}), \mathbf{q}_i(k_p^{(m)}))$.
3. **Detect degenerate subspaces.** For each $k_p^{(m)}$, cluster eigenvalues that are equal (within a tolerance) and whose corresponding eigenvectors have negligible coupling $\mathbf{q}_i^H \mathbf{K}' \mathbf{q}_j$. Each cluster forms a degenerate subspace \mathcal{S} of dimension $d > 1$. This detection determines whether to use pointwise MAC (for non-degenerate modes) or subspace MAC (for degenerate subspaces) in the subsequent steps.
4. **Build cost matrix.** For each interval $[k_p^{(m)}, k_{p+1}^{(m)}]$, construct a cost matrix \mathbf{C} of size $M \times N$ (or subspace-to-subspace) with entries $C_{ij} = 1 - \text{MAC}$ (or $1 - \text{MAC}_{\text{sub}}$). This matrix quantifies the dissimilarity between objects at the two wavenumbers.
5. **Optimal mode assignment.** Apply the Hungarian algorithm (also known as the Munkres assignment algorithm) to find the permutation σ that minimizes the total cost, i.e., the sum of $C_{i,\sigma(i)}$. This yields the globally optimal matching of modes (or subspaces) between $k_p^{(m)}$ and $k_{p+1}^{(m)}$.
6. **Compute MAC separation and error indicator.** For each matched object, compute the MAC separation $D_i(k_p^{(m)}, \Delta k_p^{(m)})$ using Eq. (22) (or its subspace analogue). Then evaluate the interval error indicator ε using Eq. (23), where the minimum is taken over all objects (modes or subspaces) in the interval.
7. **Check refinement condition.** If $\varepsilon(k_p^{(m)}, \Delta k_p^{(m)}) > \bar{\varepsilon}$ and $\Delta k_p^{(m)} > \Delta k_{\min}$, mark the interval for refinement.

8. **Refine grid.** For each marked interval, insert a new grid point at its midpoint:

$$k_{mid} = \frac{k_p^m + k_{p+1}^m}{2}. \quad (28)$$

Increment $m \leftarrow m + 1$, update the grid: $\mathbf{k}^{(m)} = \mathbf{k}^{(m-1)} \cup k_{mid}$, return to Step 2.

9. **Convergence.** When no interval satisfies the refinement condition, the algorithm terminates. The final grid $\mathbf{k}^{(m)}$ and the corresponding eigen-solutions are output.

10. **Output.** The algorithm produces a sorted modal dataset \mathcal{D} as sampled wavenumber increases.

The flowchart in Fig. 1 visually encapsulates this iterative refinement loop.

2.8.2 Discussion and implementation details

Choice of tolerance $\bar{\varepsilon}$. Theorem 1 guarantees that for sufficiently small Δk the error indicator ε can be made arbitrarily close to 0. In practice, a tolerance of $\bar{\varepsilon} = 0.05$ (i.e., requiring $1 - \min_i D_i \leq 0.05$, hence $\min_i D_i \geq 0.95$) has proven effective in numerical experiments. Larger values lead to more conservative (finer) grids, while smaller values risk accepting ambiguous mode pairings. The choice may be adjusted based on the desired safety margin and computational budget.

Why the algorithm works. Consider any interval $[k_p, k_{p+1}]$ that survives the refinement loop. By construction, $\varepsilon(k_p, \Delta k_p) \leq \bar{\varepsilon}$, which implies $\min_i D_i \geq 1 - \bar{\varepsilon} > 0$. Hence the correct tracking condition Eq. (19) holds for every mode i on that interval, and mode identities are unambiguously preserved across the whole dispersion curve. Moreover, intervals that initially exhibited large ε have been recursively halved until either ε falls below $\bar{\varepsilon}$ or the step size reaches Δk_{\min} . Thus the final step sizes in veering regions are guaranteed to be smaller than the local $\Delta k_{\max}(k)$ (up to the limitation imposed by machine precision). The algorithm therefore automatically adapts to the local eigenvector sensitivity.

Bidirectional consistency. The definition of $D_i(k, \Delta k)$ in Eq. (22) explicitly incorporates both row-wise and column-wise conditions by taking the minimum of D_i^{row} and D_i^{col} . Consequently, the error indicator $\varepsilon(k, \Delta k) = 1 - \min_i D_i(k, \Delta k)$ simultaneously monitors forward tracking confidence (from k_p to k_{p+1}) and backward tracking confidence (from k_{p+1} to k_p). If $\varepsilon(k_p, \Delta k_p) \leq \bar{\varepsilon}$, it guarantees that both the row and column conditions are satisfied for all modes, i.e., the identity permutation is the unique optimal matching in both directions. No additional backward sweep is required, as the error indicator already accounts for bidirectional consistency by construction. This unified treatment simplifies the algorithm while maintaining robustness against non-monotonic eigenvector variations or asymmetric mode shapes.

Relation to existing software. Commonly used tools for guided wave dispersion (e.g., SAFEDC, GUIGUW, Dispersion Calculator) typically rely on uniform sampling or require the user to manually refine regions of interest. To the best of our knowledge, no automatic, MAC-based adaptive refinement strategy has been implemented in these codes. The proposed algorithm fills this gap and can be integrated into any SAFE solver with minimal effort.

2.8.3 Convergence and practical considerations

The refinement process terminates because each marked interval is bisected, so the step sizes in problematic regions decrease geometrically. Theorem 1 guarantees that after a finite number of bisections the step will fall below $\Delta k_{\max}(k)$ and ε will become arbitrarily small, provided machine precision does not intervene. In practice, the minimum step Δk_{\min} acts as a safeguard against infinite

loops; if an interval reaches Δk_{\min} and still exhibits $\varepsilon > \bar{\varepsilon}$, the algorithm flags it as potentially unresolvable (e.g., due to numerical noise or an extremely narrow veering). The user may then decide whether to accept the result or to increase numerical precision.

The computational overhead of the adaptive procedure is moderate: each refinement step solves eigenvalue problems only at the newly inserted points, not at all grid points anew. The total number of solves is proportional to the final number of grid points, which is typically much smaller than the number that would be required by a uniformly fine grid covering the whole range. Efficiency gains are most pronounced when veering regions occupy only a small fraction of the wavenumber domain—a common situation in practice.

In summary, the adaptive wavenumber sampling algorithm provides a mathematically grounded, practical tool for robust mode tracking in SAFE dispersion analysis. It leverages the theoretical existence of a sufficiently small step (Theorem 1) and translates it into a concrete, automated refinement scheme driven by the easily computable error indicator $\varepsilon(k, \Delta k)$.

3 Numerical results

This section presents a thorough numerical validation of the proposed adaptive wavenumber sampling algorithm. The primary objectives are twofold: first, to demonstrate the algorithm’s capability to accurately track modes in both symmetry-protected crossings and avoided crossings (veering); second, to evaluate its computational efficiency in comparison with existing methods. Four numerical examples covering a diverse range of waveguide geometries and material configurations have been selected: a symmetric laminated composite plate, an unsymmetric laminated composite plate, an L-shaped aluminum bar, and a steel pipe. All waveguides are assumed to have traction-free boundary conditions.

The performance of our method is benchmarked against two open-source implementations: SAFEDC [27], a SAFE-based dispersion calculator, and the Dispersion Calculator (DC) [26], which employs a stiffness matrix formulation. Both tools are implemented in MATLAB and represent distinct strategies for mode tracking.

SAFEDC constructs dispersion curves by solving the SAFE eigenvalue problem on a uniformly spaced wavenumber grid and subsequently applying a classical MAC-based mode tracking procedure. While straightforward, this uniform sampling approach is susceptible to mode misidentification in veering regions where the eigenvector variation outpaces the fixed step size, as will be demonstrated in the following examples.

DC adopts a fundamentally different philosophy. By exploiting the symmetry and coupling properties of the laminate, it first partitions modes into distinct families—such as Lamb, shear horizontal, and Scholte waves. For each selected family, a mode-by-mode extraction strategy is employed: using a user-defined fixed frequency step, the software traces each mode independently by solving the characteristic equation at every discrete frequency point. The solution at the preceding step serves as an initial estimate for the next step, ensuring curve continuity through a predictor-corrector mechanism. Although the exact numerical implementation is not publicly disclosed, this continuation-based strategy enables robust extraction of dispersion curves for multilayered anisotropic plates, albeit at the cost of requiring fine frequency steps and careful initialization.

The selection of these two comparison tools is deliberate. Comparison with SAFEDC highlights the limitations of uniform sampling and the benefits of adaptive refinement. Comparison with DC validates the accuracy of the proposed MAC-based tracking in veering and crossing regions against a

well-established continuation method. Together, these comparisons underscore the advantages of the adaptive algorithm in terms of both tracking reliability and computational economy.

For all numerical examples, the system matrices \mathbf{K}_1 , \mathbf{K}_2 , \mathbf{K}_3 , and \mathbf{M} are normalized using a characteristic length a and a characteristic wave velocity c_T . Consequently, all reported quantities (wavenumber, frequency, phase velocity) are dimensionless. This normalization ensures numerical stability and facilitates consistent parameter selection across examples. The material properties, characteristic length a , and characteristic wave velocity c_T for each example are summarized in Table 2.

Table 2: Material properties, characteristic length a and characteristic wave velocity c_T for the four numerical examples.

Example	Material	Isotropy	Properties	Length a	Velocity c_T
Symmetric laminate Unsymmetric laminate	M21T800	Transversely isotropic	$E_1 = 171$ GPa, $E_2 = 11.47$ GPa, $G_{12} = 4.83$ GPa, $\rho = 1600$ Kg/m ³ , $\nu_{12} = 0.33$, $\nu_{23} = 0.33$	Half laminate thickness	3000 m/s
L-shaped bar	Aluminium	Isotropic	$E = 70$ GPa, $\nu = 0.33$, $\rho = 2700$ Kg/m ³	Half short leg length	3040 ¹ m/s
Steel pipe	Steel	Isotropic	$E = 207$ GPa, $\nu = 0.3$, $\rho = 7850$ Kg/m ³	Half radial thickness	3000 m/s

¹ The same c_T is used as in Ref. [42] for comparison purposes.

The adaptive algorithm is configured with the following parameters, chosen based on extensive preliminary experiments:

- Mesh discretisation: For the plate structures (laminates), Gauss–Lobatto–Legendre (GLL) elements with GLL quadrature are employed to maximise the sparsity of the mass matrix \mathbf{M} , with the same implementation as in SAFEDC. For the two-dimensional cross-sections (L-shaped bar and steel pipe), nine-node quadrilateral (quad9) elements with Gaussian quadrature are used.
- Tolerance: $\bar{\varepsilon} = 0.05$, requiring the error indicator (defined in Eq. (23)) to fall below 5% for acceptance. This relatively stringent tolerance ensures high confidence in mode identification.
- Minimum step size: $\Delta k_{\min} = 10^{-3}$, safeguarding against infinite refinement due to numerical noise or extremely narrow veering regions.
- Initial grid: Uniform sampling with 10 points per unit normalized wavenumber ($\Delta k = 0.1$), providing a coarse baseline that reveals regions requiring refinement.
- Refinement criterion: An interval $[k_p, k_{p+1}]$ is marked for refinement if $\varepsilon(k_p, \Delta k_p) > \bar{\varepsilon}$ and $\Delta k_p > \Delta k_{\min}$.

At each refinement iteration, error indicators are recomputed for all refinement intervals, and the process continues until convergence or until the minimum step size is reached. The following subsections detail the four validation cases, each illustrating different aspects of the algorithm’s performance.

It is worth noting that our SAFE formulation, eigenvalue solver, and adaptive sampling algorithm were developed in a Python environment, whereas SAFEDC and DC are MATLAB-based. Thus, validating the proposed adaptive sampling strategy also serves to verify the correctness of our SAFE implementation from the material property level up to the final dispersion curves.

3.1 Symmetric laminated plate: symmetry-protected crossings

The first validation case considers a symmetric laminated composite plate, a configuration that serves to demonstrate the algorithm’s behaviour in the presence of symmetry-protected crossings. Due to the layup symmetry, modes belonging to different symmetry classes—namely symmetric (S) and antisymmetric (A) modes—remain uncoupled throughout the wavenumber range. According to the Wigner–von Neumann non-crossing rule discussed in Section 2.5, such symmetry-protected crossings should be trackable even with relatively coarse sampling, as the coupling term $\mathbf{q}_j^H \mathbf{K}' \mathbf{q}_i$ vanishes identically, ensuring bounded eigenvector derivatives.

The laminate is composed of M21/T800 carbon-epoxy laminae (individual ply thickness: 0.25 mm) with a stacking sequence of $[0, 90, 45, -45]_{2s}$. The complete lamina material properties are provided in Table 2. The symmetric layup decouples the symmetric and antisymmetric wave families, creating a well-structured modal spectrum ideal for benchmarking.

Fig. 2 compares the dispersion curves (ω versus k) obtained from four approaches: (a) the proposed adaptive method on the initial coarse grid ($\Delta k = 0.1$), (b) the adaptive method after refinement, (c) SAFEDC with uniform fine sampling ($\Delta k = 0.02$), and (d) the DC with fixed frequency step ($\Delta \omega = 0.0209$), where symmetric modes are plotted in blue, antisymmetric modes in red.

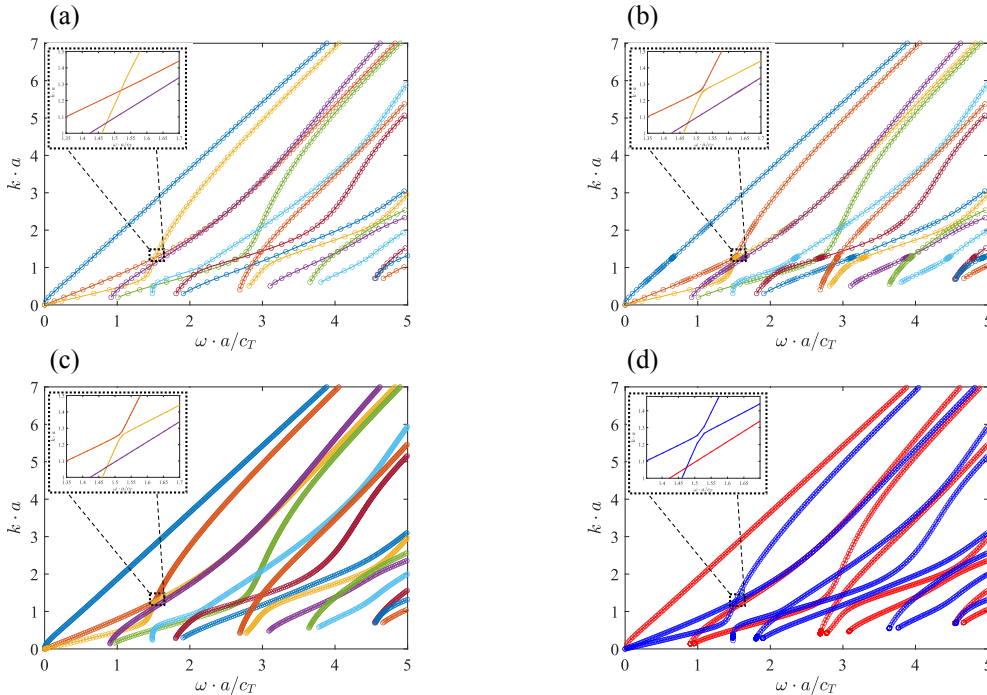


Figure 2: Dispersion curves (dimensionless frequency ω versus dimensionless wavenumber k) for the symmetric laminated plate $[0, 90, 45, -45]_{2s}$: (a) initial coarse sampling ($\Delta k = 0.1$, 70 points) showing mode misidentification in the veering region (black square) due to insufficient resolution; (b) adaptive refinement result (98 points) correctly tracking all modes after automatic refinement guided by the error indicator; (c) SAFEDC with dense uniform sampling ($\Delta k = 0.02$, 350 points) resolving the veering but at high computational cost; (d) Dispersion Calculator (DC) results ($\Delta \omega = 0.0209$) confirming the absence of crossings within each symmetry family and validating the veering structure. Symmetric modes (S) are shown in blue, antisymmetric modes (A) in red. The inset in (d) reveals the avoided crossing between two S-mode branches.

Several observations emerge from this comparison. First, the DC results in Fig. 2(d) confirm that within each mode family (S or A), true eigenvalue crossings are absent—a direct consequence of the Wigner–von Neumann theorem for modes sharing the same symmetry class. The region marked by a black square, where two S-mode branches appear to intersect, reveals upon closer inspection (inset) a

classical avoided crossing (veering) between modes of the same symmetry. DC’s family-splitting and continuation-based tracking successfully resolves this veering.

Second, the coarse initial sampling (Fig. 2(a)) correctly tracks all crossings between different symmetry classes (S–A intersections), as predicted by theory. However, the same coarse sampling fails to correctly identify the two S-mode branches through the veering region, resulting in a mode mis-assignment. This failure illustrates the fundamental limitation of uniform sampling in veering zones: when the eigenvalue gap becomes small, the eigenvector variation over a fixed step Δk exceeds the local critical step $\Delta k_{\max}(k)$, violating the tracking condition Eq. (19).

Third, SAFEDC with dense uniform sampling (Fig. 2(c), $\Delta k = 0.02$) resolves the veering correctly, demonstrating that a sufficiently fine grid can overcome the difficulty. However, this comes at a cost: the number of sampling points increases from 70 (coarse) to 350 (fine), and the uniform refinement provides no indication of where refinement is actually needed or whether the resulting mode assignments are reliable.

The proposed adaptive algorithm addresses both limitations. Fig. 3(a) shows the error indicator $\varepsilon(k, \Delta k)$ before and after refinement. On the initial grid, a pronounced peak appears precisely in the veering region ($k \in [0.4, 2.1]$), with ε exceeding the tolerance $\bar{\varepsilon} = 0.05$. This peak signals that the local step size exceeds $\Delta k_{\max}(k)$, triggering automatic refinement. After inserting additional points in this region, the error indicator falls uniformly below the tolerance, indicating that all intervals now satisfy the correct tracking condition. Consequently, as shown in Fig. 2(b), the adaptive refinement successfully resolves the mode veering that was misidentified under coarse sampling. The final grid contains 98 points—modestly higher than the coarse grid (70 points) but substantially fewer than the 350 points required by uniform fine sampling. Crucially, the algorithm provides quantitative confidence: the post-refinement error indicators confirm reliable mode identification across the entire wavenumber range.

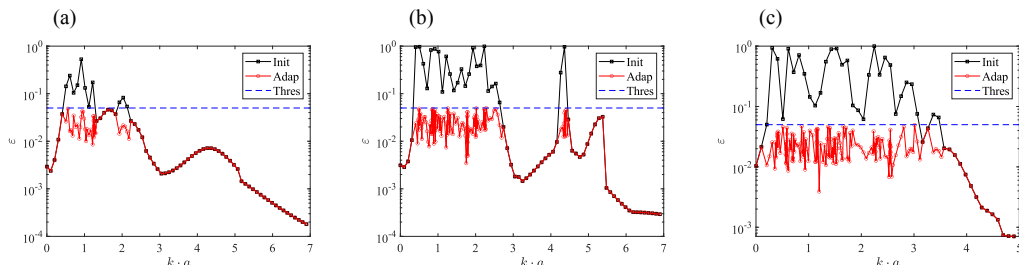


Figure 3: Error indicator $\varepsilon(k, \Delta k)$ before and after adaptive refinement for all three validation cases: (a) symmetric laminate, (b) unsymmetric laminate, (c) L-shaped bar. In every example, the refinement systematically reduces ε below the tolerance $\bar{\varepsilon} = 0.05$ across the entire wavenumber range, demonstrating that the adaptive algorithm successfully identifies and resolves all regions where the initial step size exceeded the local critical threshold $\Delta k_{\max}(k)$. The post-refinement error indicators provide quantitative confirmation that the correct tracking condition Eq. (19) holds for all modes and all intervals.

This example demonstrates three key capabilities of the proposed method: (i) it correctly handles symmetry-protected crossings without special treatment; (ii) it automatically detects veering regions where the step size is inadequate; and (iii) it refines only where necessary, achieving tracking accuracy comparable to dense uniform sampling with significantly fewer eigenvalue solves. The error indicator serves both as a refinement driver and as an a posteriori quality measure—a feature absent in conventional approaches.

3.2 Unsymmetric laminated plate: pervasive veering

The second example considers an unsymmetric laminated plate, which exhibits pervasive avoided crossings (veering) due to the absence of through-thickness symmetry. This configuration provides a stringent test for mode tracking algorithms, as eigenvalue gaps become extremely small and eigenvectors undergo rapid variation over narrow wavenumber intervals.

The laminate is again composed of M21/T800 carbon–epoxy laminae (individual ply thickness: 0.25 mm), with a stacking sequence of $[0, 90, 45, -45]_4$. The lack of symmetry introduces coupling phenomena such as tension–shear and bending–torsion coupling. Consequently, pure symmetric (S), antisymmetric (A), and shear horizontal (SH) modes do not exist; instead, all modes are mixed. According to the Wigner–von Neumann non-crossing rule (Section 2.5), no true eigenvalue crossings are expected in this unsymmetric configuration, as the absence of symmetry protection forces all modal interactions to be of the avoided-crossing type.

Fig. 4 compares the dispersion curves (ω versus dimensionless wavenumber k) obtained from four approaches: (a) the proposed adaptive method on the initial coarse grid ($\Delta k = 0.1$, 70 points); (b) the adaptive method after refinement; (c) SAFEDC with uniform fine sampling ($\Delta k = 0.02$, 350 points); and (d) the Dispersion Calculator (DC) with a fixed frequency step ($\Delta\omega = 0.0209$).

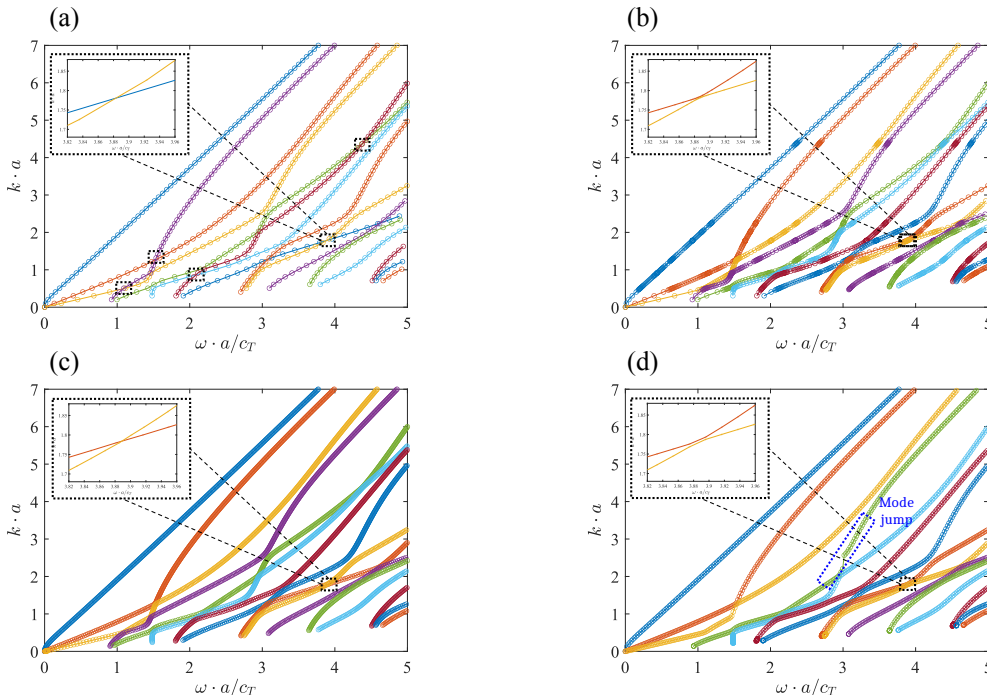


Figure 4: Dispersion curves (ω versus k) for the unsymmetric laminated plate $[0, 90, 45, -45]_4$: (a) initial coarse sampling ($\Delta k = 0.1$, 70 points) exhibiting multiple mode misidentifications (black squares) due to insufficient resolution in veering regions; (b) adaptive refinement result (185 points) correctly tracking all modes after automatic refinement guided by the error indicator; (c) SAFEDC with dense uniform sampling ($\Delta k = 0.02$, 350 points) reducing but not eliminating tracking errors (one remaining misidentification); (d) DC results ($\Delta\omega = 0.01045$) confirming the absence of true crossings among all coupled modes, but failing to detect all modes (one modes missing).

On the initial coarse grid (Fig. 4(a)), multiple mode misidentifications occur, highlighted by black squares. These regions correspond to veering zones where the local eigenvector gradient $|\mathbf{q}i'| \mathbf{M}$ is large, as predicted by the derivative expansion Eq. (10). The coarse step size $\Delta k = 0.1$ exceeds the local critical step $\Delta k_{\max}(k)$ in these intervals, violating the correct tracking condition Eq. (19).

Increasing the sampling resolution uniformly to $\Delta k = 0.02$ (SAFEDC, Fig. 4(c)) reduces the num-

ber of misidentifications to one, but does not eliminate them entirely. This residual error underscores a fundamental limitation of uniform sampling: unless the step size is chosen smaller than the minimum of $\Delta k_{\max}(k)$ over the entire wavenumber range—a value that is unknown a priori and may be extremely small in the most severe veering region—some misidentifications will persist. Determining such a globally sufficient resolution is impractical and computationally prohibitive, as it would require an excessively fine grid everywhere.

The DC results (Fig. 4(d)) confirm the complete absence of true crossings, consistent with the Wigner–von Neumann rule. However, DC fails to detect all modes in this unsymmetric configuration. Even with a refined frequency step ($\Delta f = 0.025$ kHz), one mode remains missing. This limitation arises from DC’s mode-detection stage, which relies on symmetry-based family separation; the strong coupling in unsymmetric laminates renders such pre-partitioning ineffective. Furthermore, the missing mode in the initial detection stage compromises the subsequent mode-by-mode tracking, causing the tracking algorithm to erroneously jump from a detected mode to the missing one. This behaviour is illustrated in the blue box in Fig. 4(d), where a mode branch is seen to deviate from its intended path. The example thus demonstrates that even sophisticated continuation methods can struggle when modes are strongly mixed, underscoring the need for more robust, detection-free tracking strategies such as the adaptive approach proposed herein.

In contrast, the proposed adaptive strategy overcomes both challenges. Fig. 3(b) shows the error indicator $\varepsilon(k, \Delta k)$ before and after refinement for this unsymmetrical laminate. On the initial grid, ε exhibits pronounced peaks in the veering regions, notably in the wavenumber intervals $[0.3, 2.6]$, and $[4.1, 4.5]$, where it exceeds the tolerance $\bar{\varepsilon} = 0.05$. These peaks signal intervals where refinement is needed. After recursive bisection in these zones, the error indicator falls uniformly below $\bar{\varepsilon}$, confirming that all intervals now satisfy the correct tracking condition. The final grid contains 185 points—half to the dense uniform grid of SAFEDC (350 points) but with the crucial difference that all modes are correctly tracked, as can be seen in Fig. 4(b). Moreover, the algorithm automatically concentrates points where they are most needed, avoiding wasteful refinement in regions where the error is already low.

This example demonstrates that the adaptive algorithm successfully navigates pervasive veering without prior knowledge of mode families or critical step sizes. It automatically identifies regions where $\Delta k_{\max}(k)$ is small, refines them until the error indicator is satisfied, and provides quantitative assurance of tracking reliability. Compared to uniform fine sampling, it achieves equivalent or superior accuracy with a comparable number of points, but with the added guarantee that all veering regions are adequately resolved.

3.3 L-shaped bar: arbitrary cross-section

To demonstrate that the adaptive strategy extends beyond plate geometries to waveguides with arbitrary cross-section—a key capability of the SAFE method—we consider an L-shaped aluminum bar. The cross-sectional geometry is depicted in Fig. 5(a). This example was recently studied by Maruyama et al. [42], who compared the numerical continuation method (NCM) with uniform-sampling SAFEDC and provided benchmark dispersion curves. Their NCM results (Fig. 7 in Ref. [42]), which track modes individually, revealed that the L-shaped bar exhibits pervasive mode veering and no true eigenvalue crossings. This behaviour is consistent with the Wigner–von Neumann non-crossing rule (Section 2.5), as the cross-section lacks the reflection symmetries that could give rise to symmetry-protected intersections.

Fig. 5 compares the dispersion curves (ω versus dimensionless wavenumber k) obtained from three

approaches: (b) the proposed adaptive method on the initial coarse grid ($\Delta k = 0.1$, 50 points); (c) the adaptive method after refinement; and (d) SAFEDC with uniform fine sampling ($\Delta k = 0.02$, 250 points). The NCM results are used as a reference to assess tracking accuracy.

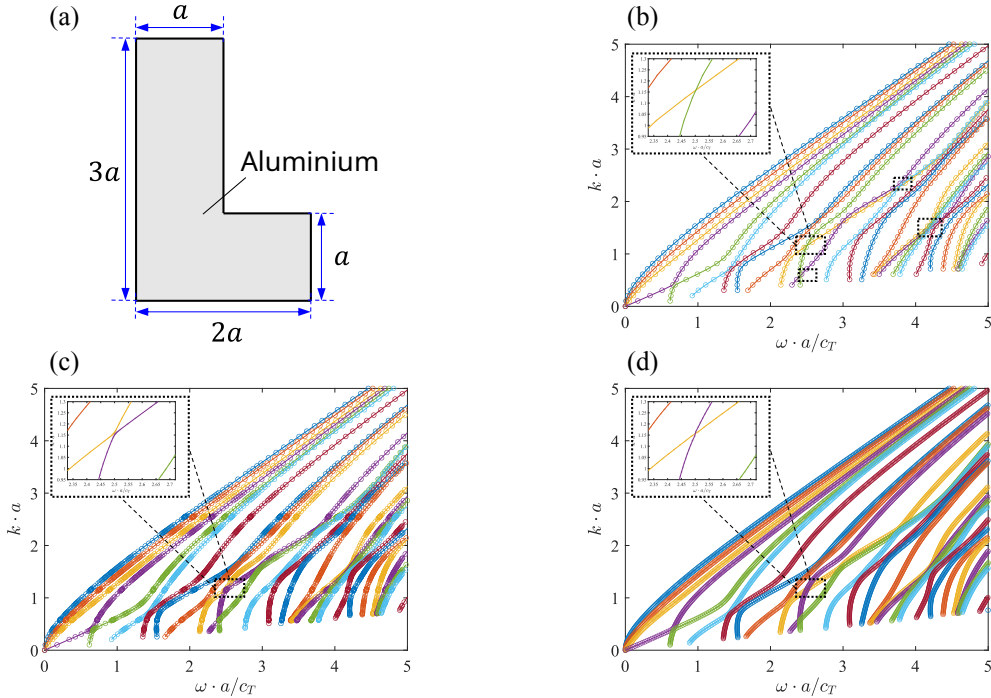


Figure 5: Dispersion curves for the L-shaped aluminum bar: (a) cross-section geometry; (b) initial coarse sampling ($\Delta k = 0.1$, 50 points) – multiple misidentifications (black squares) occur in veering regions; (c) adaptive refinement (191 points) – all modes correctly tracked after error-driven refinement; (d) SAFEDC with dense uniform sampling ($\Delta k = 0.02$, 250 points) – reduces but does not eliminate misidentifications (circled residual error). The reference NCM (Fig. 7 in Ref. [42]) confirms the absence of true crossings, making veering the sole source of tracking difficulty. Adaptive sampling achieves perfect tracking with fewer points than uniform fine sampling.

On the initial coarse grid (Fig. 5(b)), several mode misidentifications are visible (marked by black squares). These occur in veering regions where the eigenvector gradient is large, and the fixed step $\Delta k = 0.1$ exceeds the local critical step $\Delta k_{\max}(k)$. SAFEDC with dense uniform sampling (Fig. 5(d)) reduces the number of misidentifications but does not eliminate them completely; one erroneous branch remains (circled). This residual error illustrates the inherent limitation of uniform sampling: without prior knowledge of the most severe veering, a globally fine grid may still under-resolve some intervals.

The adaptive algorithm overcomes this difficulty by concentrating points where they are most needed. Fig. 3(c) displays the error indicator $\varepsilon(k, \Delta k)$ before and after refinement. On the initial grid, ε shows pronounced peaks in the veering regions, most notably in the wavenumber interval $[0.2, 3.4]$, where it exceeds the tolerance $\bar{\varepsilon} = 0.01$. These peaks signal intervals requiring refinement. After recursive bisection in these zones, the error indicator falls uniformly below $\bar{\varepsilon}$, confirming that the correct tracking condition Eq. (19) now holds for all modes. All inaccurate crossings in the initial sparse sampling are corrected as mode veering after adaptive refinement, as shown in Fig. 5(c). The final grid contains 191 points—fewer than the 250 points used by uniform fine sampling—yet achieves perfect tracking with no misidentifications.

This example confirms that the adaptive strategy works reliably for arbitrary cross-sections, automatically identifying and refining veering regions without any prior knowledge of the modal structure.

The error indicator provides quantitative assurance that all intervals are adequately resolved, a feature absent from conventional uniform-sampling approaches.

3.4 Steel pipe: closed-section waveguide with symmetry-protected degeneracy

To further demonstrate the applicability of the proposed adaptive strategy to waveguides exhibiting symmetry-protected degeneracy, we consider a steel pipe with inner radius $13a$ and outer radius $15a$ (where a is a characteristic length). For an ideal axisymmetric waveguide, one may formulate the problem in a cylindrical coordinate system (r, θ, z) and assume a harmonic wave propagation of the form $\mathbf{u}(r, \theta, z, t) = \mathbf{N}(r)\mathbf{q}e^{i(kz+m\theta-\omega t)}$, where $m = 0, 1, 2, \dots$ is the circumferential order [49]. This formulation decouples the problem for each m , allowing dispersion curves to be computed separately for each circumferential family. In the present work, however, we deliberately compute the dispersion curves using a full three-dimensional Cartesian SAFE model of the pipe cross-section. This approach captures all circumferential orders simultaneously, providing a more stringent test of the mode tracking algorithm, which must correctly identify and separate modes belonging to different m families without prior knowledge of the underlying symmetry.

The axisymmetry of the structure manifests as rotational invariance, a continuous symmetry that profoundly influences its modal structure. As a consequence, for each circumferential order $m > 0$, two orthogonal modes of the form $\sin(m\theta)$ and $\cos(m\theta)$ coexist and share exactly the same eigenvalue for all axial wavenumbers k . These two modes constitute a symmetry-protected degenerate pair. The coupling term $\mathbf{q}_j^H \mathbf{K}' \mathbf{q}_i$ vanishes identically due to symmetry, yet the eigenvectors are not uniquely defined. Instead, they span a two-dimensional invariant subspace in which any orthonormal basis is admissible; any linear combination of the two degenerate modes remains a valid eigenvector corresponding to the same eigenvalue. A detailed theoretical discussion of symmetry-protected degeneracy is provided in Section 2.7.

This non-uniqueness poses a fundamental challenge for pointwise MAC tracking. Even though the eigenvalues vary continuously with k , the computed basis vectors within the degenerate subspace may rotate arbitrarily between neighbouring wavenumbers due to minor numerical perturbations. Consequently, conventional pointwise MAC tracking may yield low confidence despite the underlying physical modes being continuous.

Fig. 6 presents the dispersion curves for the steel pipe obtained using three approaches: (b) initial coarse sampling ($\Delta k = 0.1$, 100 points); (c) the proposed adaptive refinement (201 points); and (d) SAFEDC with dense uniform sampling ($\Delta k = 0.04$, 250 points). All three approaches produce identical dispersion curves, confirming the accuracy of the adaptive strategy. For each circumferential order $m > 0$, the $\sin(m\theta)$ and $\cos(m\theta)$ modes collapse onto the same dispersion branch. Moreover, multiple symmetry-protected crossings occur between different circumferential orders; these crossings are permitted by symmetry and do not lead to mode veering.

More revealing insights emerge from examining the mode-tracking error indicators. Fig. 7 compares the tracking error before and after adaptive refinement using two different similarity measures: (a) pointwise MAC and (b) subspace MAC (defined in 2.7).

When pointwise MAC is employed, the error ε cannot be reduced below the prescribed threshold $\bar{\varepsilon}$ in the low- k regime, even after multiple refinement iterations. This behaviour does not indicate a physical discontinuity in the dispersion branches. Rather, it reflects the strong rotation of the two-dimensional degenerate subspace between neighbouring wavenumbers. In the low- k regime, the SAFE stiffness matrix $\mathbf{K}(k) = \mathbf{K}_1 + ik\mathbf{K}_2 + k^2\mathbf{K}_3$ is dominated by the k -independent term \mathbf{K}_1 . Small

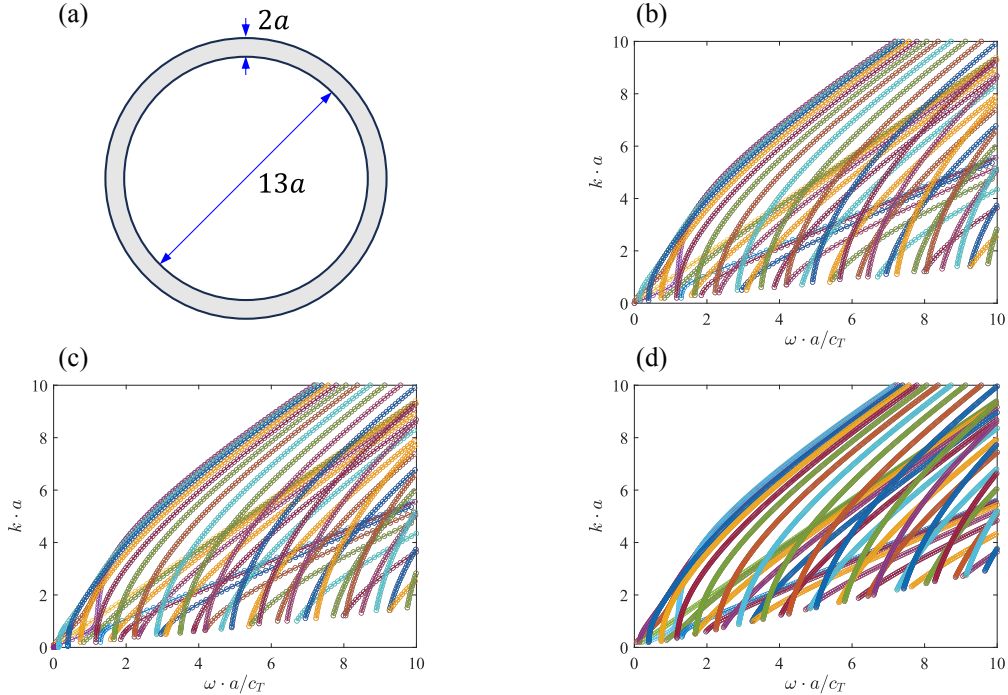


Figure 6: Dispersion curves for a steel pipe: (a) cross-section geometry; (b) initial coarse sampling ($\Delta k = 0.1$, 100 points); (c) adaptive refinement (201 points); (d) SAFEDC with dense uniform sampling ($\Delta k = 0.04$, 250 points). For each circumferential wavenumber $m > 0$, a degenerate pair arises from symmetry-protected degeneracy, producing coincident dispersion branches. All three sampling strategies yield identical curves, validating the adaptive method’s accuracy.

variations in k lead to relatively significant changes in the relative contributions of \mathbf{K}_1 , \mathbf{K}_2 , and \mathbf{K}_3 , making the degenerate subspace more sensitive to perturbations. Consequently, the computed basis vectors of the degenerate pair may rotate substantially between adjacent k steps, causing low pointwise MAC confidence even though the subspace itself evolves smoothly.

In contrast, in the high- k regime, the k -dependent terms—particularly $k^2\mathbf{K}_3$ —dominate the stiffness matrix. The relative influence of \mathbf{K}_1 diminishes, and the spectral structure is primarily governed by the high-order terms. As a result, the degenerate subspace varies more smoothly with respect to k , and the basis rotation between adjacent wavenumbers becomes small. This explains why pointwise MAC confidence is naturally high at high k , even under coarse sampling.

To overcome the intrinsic limitation of pointwise MAC in the presence of symmetry-protected degeneracy, the adaptive algorithm detects degenerate eigenvalue clusters on the coarse grid and switches to subspace MAC tracking, as illustrated in Fig. 1. In this framework, each degenerate pair is treated as a single physical entity represented by its invariant subspace, rather than attempting to track the two basis vectors individually. The subspace MAC, defined in Eq. (24), provides a rotation-invariant measure of similarity between subspaces. By matching subspaces instead of individual vectors, the tracking process becomes robust to arbitrary basis rotations within the degenerate subspace. Consequently, after adaptive refinement guided by subspace MAC, the error indicator ε is successfully reduced below the threshold $\bar{\varepsilon}$ across the entire wavenumber range (Fig. 7(b)).

The steel pipe example highlights a fundamental limitation of pointwise MAC tracking in the presence of symmetry-protected degeneracy: low confidence in the low- k regime does not reflect physical mode discontinuity, but rather the non-uniqueness and rotation of degenerate eigenvectors. By recognising each degenerate pair as a unified invariant subspace and employing subspace MAC for tracking, the proposed adaptive strategy achieves robust and high-confidence mode tracking over

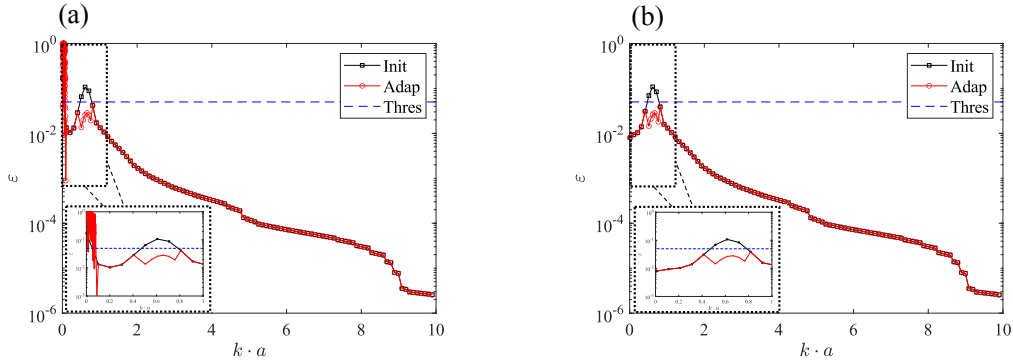


Figure 7: Error indicator $\varepsilon(k, \Delta k)$ before and after adaptive refinement: (a) pointwise MAC tracking, which fails to reduce the error below the threshold $\bar{\varepsilon}$ in the low- k regime; (b) subspace MAC tracking, where each degenerate pair is treated as a two-dimensional invariant subspace. After adaptive refinement guided by subspace MAC, the error falls uniformly below $\bar{\varepsilon}$.

the full dispersive spectrum. This confirms that the method remains effective even for closed-section waveguides with strong rotational symmetry and pervasive degeneracy.

4 Discussion

The numerical examples presented in [Section 3](#) demonstrate the effectiveness of the proposed adaptive wavenumber sampling algorithm across a diverse set of waveguides. In this section, we discuss the implications of these results, analyze the computational efficiency of the method, and highlight its advantages in the context of existing approaches.

4.1 Computational efficiency

A primary motivation for adaptive sampling is to concentrate computational effort where it is most needed—namely, in regions where the eigenvector gradient $\|\mathbf{q}'_i\|_{\mathbf{M}}$ is large. The total cost of the algorithm is proportional to the number of eigenvalue solves performed. Each refinement iteration adds solves only at the newly inserted points, so the final number of solves equals the number of points in the adapted grid.

[Table 3](#) summarises the grid sizes for the five examples. In all cases, the adaptive grid contains significantly fewer points than a uniformly fine grid that would be required to achieve comparable accuracy (e.g., the dense uniform sampling used in SAFEDC). The savings are most pronounced when veering regions occupy only a small fraction of the wavenumber domain—a common situation in practice. For the symmetric laminate, the adaptive grid used 98 points versus 350 for uniform fine sampling; for the unsymmetric laminate, 185 points versus 350. The L-shaped bar required 191 points versus 250, and the steel pipe 201 points versus 250. These reductions directly translate into lower computational time, especially when repeated solves are needed for parametric studies or optimisation.

An additional advantage of the SAFE formulation is that eigenvalue problems at different wavenumbers are independent. This makes the algorithm trivially parallelisable: solves on the initial grid and on each refinement level can be distributed across multiple processors. In our Python implementation, parallelisation over wavenumber points reduced the wall-clock time by a factor approximately equal to the number of cores. Such scalability is essential for large-scale problems or when high accuracy demands many grid points.

Table 3: Comparison of grid sizes for the numerical examples.

Example	Coarse initial	Adaptive final	Uniform fine (SAFEDC)
Symmetric laminate	70	98	350
Unsymmetric laminate	70	185	350
L-shaped bar	50	191	250
Steel pipe	100	201	250

4.2 Comparison with continuation-based methods

Continuation methods [42] employ a mode-by-mode strategy that traces each dispersion branch independently using a predictor–corrector scheme. While robust and accurate in many settings, this approach has several inherent limitations.

To maintain corrector convergence, continuation methods must adapt the step size based on estimates of the solution curvature or the condition number of the Jacobian. In veering regions, where the eigenvector gradient is large, this requirement forces the step size to be reduced—often by bisection—analogous to the refinement performed by our adaptive algorithm when the MAC separation falls below the tolerance. Both strategies therefore share the concept of local step size control guided by an indicator of solution variability.

However, several fundamental limitations distinguish continuation methods from the proposed approach. First, they require a user-supplied initial guess for each mode, typically obtained from a low-frequency or cut-off solution. The sensitivity of the corrector step to the quality of this initial guess makes the method less robust, particularly in dense modal spectra where mode families may interact strongly.

Second, the method is inherently sequential: each forward step depends on the previous converged solution, preventing parallelisation over the parameter domain. While different modes can be traced independently, this offers limited parallelism compared to solving eigenvalue problems, which are embarrassingly parallel across wavenumber points.

Third, and most fundamentally, continuation methods rely on the non-singularity of the Jacobian matrix of the underlying nonlinear system. In veering regions, the Jacobian becomes increasingly ill-conditioned as the eigenvalue gap decreases; in the limiting case of symmetry-protected degeneracy, the Jacobian becomes exactly singular, causing the method to break down entirely. Our subspace-tracking framework, by contrast, handles such degeneracies directly and robustly by treating the invariant subspace as a single entity, circumventing the need for a non-singular Jacobian.

In summary, while continuation methods offer a viable approach for mode tracking, they lack the mathematical guarantees, parallel scalability, and robustness to degeneracy that the proposed framework provides.

4.3 The role of the error indicator

A distinctive feature of the proposed approach is the a posteriori error indicator $\varepsilon(k, \Delta k)$. Unlike conventional methods that provide only a binary success/failure of mode assignment, our indicator quantifies the confidence of the tracking on every interval. This information can be used to:

- automatically trigger refinement,
- flag intervals where the solution may be unreliable (e.g., due to extremely narrow veering or numerical noise),

- provide users with a quality measure for the final dispersion curves.

The error indicator also enables a systematic trade-off between accuracy and computational cost via the tolerance $\bar{\varepsilon}$. In practice, $\bar{\varepsilon} = 0.1$ proved a reasonable compromise, but the optimal value may depend on the application.

4.4 Handling symmetry-protected degeneracy

The steel pipe example revealed a fundamental limitation of pointwise MAC tracking in the presence of symmetry-protected degeneracy. Because eigenvectors within a degenerate subspace are not uniquely defined, pointwise MAC can yield arbitrarily low confidence even when the underlying physics is continuous. Our solution—switching to subspace MAC and treating each degenerate pair as a single invariant subspace—preserves the mathematical structure and restores robust tracking. The subspace MAC is rotation-invariant and reduces to the standard MAC for one-dimensional subspaces, providing a unified framework. This extension broadens the applicability of the adaptive method to axisymmetric waveguides and other structures with continuous symmetries.

The observed variation in subspace stability with wavenumber—rapid rotation at low k , smooth variation at high k —is itself an interesting physical phenomenon. It arises from the changing balance between the k -independent stiffness \mathbf{K}_1 and the k -dependent terms $ik\mathbf{K}_2$ and $k^2\mathbf{K}_3$. This suggests that the required step size for accurate subspace tracking is not uniform, further justifying the need for adaptivity.

4.5 Choice of sweeping parameter: wavenumber versus frequency

An important practical consideration in dispersion analysis is whether to sweep the wavenumber k (solving for frequencies ω) or sweep the frequency ω (solving for wavenumbers k). The SAFE formulation naturally accommodates both approaches, but the choice has significant implications for the structure of the resulting eigenvalue problem and the associated computational challenges.

For undamped waveguides with time-harmonic behaviour, the stiffness matrix $\mathbf{K}(k) = \mathbf{K}_1 + ik\mathbf{K}_2 + k^2\mathbf{K}_3$ is Hermitian for real k . Sweeping k therefore yields a linear Hermitian eigenvalue problem $\mathbf{K}(k)\mathbf{q} = \omega^2\mathbf{M}\mathbf{q}$, which can be solved efficiently with standard eigensolvers that exploit Hermitian structure. Moreover, the eigenvalues ω^2 are real and the eigenvectors satisfy convenient orthogonality properties. This approach is mathematically clean, numerically stable, and directly amenable to the perturbation analysis presented in [Section 2.3](#).

In contrast, sweeping frequency leads to a quadratic eigenvalue problem $(\mathbf{K}_1 + ik\mathbf{K}_2 + k^2\mathbf{K}_3 - \omega^2\mathbf{M})\mathbf{q} = \mathbf{0}$ in the unknown wavenumber k . While this can be linearised into a larger system (typically doubling the degrees of freedom), the resulting linearised eigenproblem is no longer Hermitian, even for undamped media. The eigenvalues k may be complex (representing propagating, evanescent, or leaky waves) and their computation requires generalised non-Hermitian eigensolvers, which are more expensive and less robust than their Hermitian counterparts.

Given these considerations, sweeping wavenumber is the preferred strategy whenever the focus is on propagating modes in undamped or weakly damped waveguides. This approach preserves the Hermitian structure, simplifies the analysis, and aligns with the theoretical framework developed in this paper.

However, there are situations where sweeping frequency becomes necessary or advantageous. For viscoelastic materials, prestressed structures, or fluid-loaded waveguides, the stiffness matrix $\mathbf{K}(k)$ loses its Hermitian property due to material damping or non-conservative effects. The wavenumber

k is then generally complex, and the eigenproblem is intrinsically non-Hermitian regardless of the sweeping parameter. In such cases, sweeping frequency is often adopted because the frequency ω remains real (excitation frequency), and the resulting polynomial eigenvalue problem for k can be tackled directly with specialised solvers (e.g., contour integration or rational Krylov methods). Moreover, when the focus is on leaky waves or on the complete complex dispersion relation, sweeping frequency is the natural choice.

In summary, the choice of sweeping parameter should be guided by the physical and mathematical structure of the problem. Sweeping wavenumber is the most straightforward and accurate path for Hermitian systems, as it avoids the unnecessary complication of a non-Hermitian linearisation. Sweeping frequency becomes essential when complex wavenumbers or non-Hermitian effects are unavoidable. The adaptive algorithm developed in this work is presented for the wavenumber-sweep formulation, but its underlying principles—error estimation, refinement criteria, and subspace tracking—can be extended to frequency-sweep implementations with appropriate modifications to the perturbation analysis.

5 Conclusion and future work

This paper has presented a comprehensive theoretical and computational framework for robust mode tracking in SAFE dispersion analysis. The work was motivated by the fundamental challenge that mode veering regions—where eigenvalues become nearly degenerate and eigenvectors undergo rapid variation—cause conventional MAC-based tracking to fail when the wavenumber step exceeds a local critical threshold $\Delta k_{\max}(k)$. Through a combination of rigorous perturbation analysis, symmetry classification, and adaptive numerical strategies, we have developed a method that automatically identifies and resolves such regions, providing quantitative confidence in the resulting dispersion curves.

The main conclusions drawn from this study are summarised as follows:

- **The error indicator reliably detects veering regions.** The quantity $\varepsilon(k, \Delta k) = 1 - \min_i D_i(k, \Delta k)$ consistently identifies intervals where the eigenvector variation outpaces the current step size. Refinement driven by this indicator successfully resolves all veering zones in the tested examples, reducing the error below the prescribed tolerance $\bar{\varepsilon} = 0.1$.
- **Symmetry-protected crossings require no special treatment.** As predicted by the Wigner–von Neumann rule, modes belonging to different symmetry classes cross without coupling, and their eigenvectors vary smoothly. The adaptive algorithm correctly tracks such crossings even on the initial coarse grid, confirming the theoretical analysis.
- **Degenerate subspaces demand subspace MAC.** In axisymmetric waveguides (e.g., the steel pipe), pointwise MAC fails due to the arbitrary rotation of eigenvectors within each degenerate pair. Switching to subspace MAC—treating the pair as a single invariant subspace—restores robust tracking and reveals a wavenumber-dependent stability: the subspace rotates rapidly at low k but smoothly at high k , justifying the need for adaptivity even in degenerate settings.
- **Adaptive sampling outperforms uniform grids.** While uniform fine sampling (SAFEDC) requires dense grids (250–350 points in the examples) and still exhibits residual tracking errors in veering regions, the adaptive method produces perfectly tracked dispersion curves using

substantially fewer points (98–201 points). The savings are most pronounced when veering regions are localised—a common situation in practice.

These findings demonstrate that the proposed framework provides a unified, confidence-guided solution for mode tracking across a wide range of lossless waveguides, from laminated plates to closed-section pipes. By quantifying tracking reliability and concentrating computational effort where it is most needed, the algorithm bridges the gap between theoretical guarantees and practical applicability.

The present work is developed under the assumption of lossless materials and traction-free boundary conditions, which ensures that the stiffness matrix $\mathbf{K}(k)$ remains Hermitian. This assumption is central to the perturbation analysis, the applicability of the Wigner–von Neumann non-crossing rule, and the existence theorem employed throughout. Consequently, the method in its current form is not directly applicable to structures that result in a non-Hermitian system:

- **Viscoelastic waveguides**, where material damping introduces complex, frequency-dependent moduli, rendering $\mathbf{K}(k)$ non-Hermitian.
- **Fluid-loaded structures**, where energy exchange between the solid and surrounding fluid leads to non-Hermitian system matrices and the emergence of leaky waves with complex wavenumbers.

While the MAC may still be used heuristically in non-Hermitian contexts, the theoretical guarantees—such as the existence of a sufficiently small step $\Delta k_{\max}(k)$ and the error indicator based on MAC separation—no longer hold, and the perturbation analysis must be revisited for non-self-adjoint eigenvalue problems.

Additional limitations relate to numerical implementation. The parameter Δk_{\min} prevents infinite refinement but may halt resolution of extremely narrow veering regions; in such cases the algorithm flags the interval and the user must decide whether to accept the result or increase numerical precision. The error indicator also depends on accurate eigenvector computation; near cut-off frequencies, solver inaccuracies could contaminate the MAC values, leading to spurious or missed refinement. The choice of tolerance $\bar{\epsilon} = 0.05$, though effective across all examples, remains heuristic and may require adjustment for problems with vastly different mode densities.

Several promising directions for future research emerge from this study, addressing both the limitations identified above and opportunities for broader applicability.

- **Extension to non-Hermitian systems.** A natural and important extension is to adapt the proposed framework to viscoelastic and fluid-loaded waveguides, where $\mathbf{K}(k)$ is no longer Hermitian. This would require revisiting the perturbation analysis for non-Hermitian eigenproblems, developing appropriate similarity measures (e.g., based on left and right eigenvectors, modal energy, or power flow), and establishing an analogous existence theorem for step size control in the complex plane. Such an extension would significantly broaden the method’s applicability to practical scenarios involving material damping or fluid coupling.
- **Frequency-domain tracking.** While the current work focuses on wavenumber-domain sampling (wavenumber sweeping), many SAFE implementations prescribe frequency and solve for the complex wavenumber. Extending the adaptive concept to frequency-domain tracking would involve reformulating the perturbation analysis for quadratic (or polynomial) eigenproblems and establishing an analogous existence theorem for frequency steps. This would enable adaptive refinement in the frequency domain, complementing the wavenumber-domain approach developed here.

- **Automatic tolerance selection.** Developing data-driven or heuristic strategies for automatically selecting the tolerance $\bar{\varepsilon}$ based on local spectral properties—such as eigenvalue gaps, condition numbers, or mode density—would make the algorithm more user-independent and robust across diverse applications.
- **Hybrid spatial-spectral adaptivity.** Combining wavenumber adaptivity with *hp*-refinement of the cross-sectional finite element mesh would enable even greater efficiency for large-scale or highly heterogeneous structures. Such an approach would concentrate both spatial and spectral resolution where needed, paving the way for accurate dispersion analysis of complex waveguides with minimal computational cost.
- **Open-source implementation.** A Python-based open-source implementation of the algorithm, named “DisperPy”, will be made publicly available at <https://github.com/dongxiao96/DisperPy>. The repository includes Jupyter notebooks that reproduce all numerical examples presented in this paper, facilitating adoption, verification, and further development by the research community. A graphical user interface (GUI) is under active development to lower the barrier for practitioners who may not wish to interact directly with the code.

In summary, this work establishes a robust, theoretically grounded framework for adaptive mode tracking in SAFE dispersion analysis, offering a significant step toward fully automated and reliable guided wave dispersion curve computation. The extensions outlined above will further broaden its impact, enabling efficient and trustworthy dispersion analysis across an even wider range of materials and waveguide configurations.

A Appendix: Detailed derivation of eigenvector perturbation analysis

This appendix provides the complete step-by-step derivation of the eigenvector derivative formulas presented in Section 2.3. The derivation follows four stages: differentiation of the eigenproblem, projection onto other modes, expansion in the eigenbasis, and imposition of a phase convention.

A.1 Differentiation of the eigenproblem

Differentiating the generalized Hermitian eigenproblem $\mathbf{K}\mathbf{q}_i = \lambda_i\mathbf{M}\mathbf{q}_i$ with respect to the wavenumber k yields

$$\mathbf{K}'\mathbf{q}_i + \mathbf{K}\mathbf{q}'_i = \lambda'_i\mathbf{M}\mathbf{q}_i + \lambda_i\mathbf{M}\mathbf{q}'_i, \quad (29)$$

where the prime denotes differentiation with respect to k . Here \mathbf{K}' is the derivative of the stiffness matrix, which is well defined because $\mathbf{K}(k)$ is analytic (in fact, polynomial) in k .

A.2 Projection onto other modes

For any index $j \neq i$, left-multiply Eq. (29) by \mathbf{q}_j^H :

$$\mathbf{q}_j^H\mathbf{K}'\mathbf{q}_i + \mathbf{q}_j^H\mathbf{K}\mathbf{q}'_i = \lambda'_i\mathbf{q}_j^H\mathbf{M}\mathbf{q}_i + \lambda_i\mathbf{q}_j^H\mathbf{M}\mathbf{q}'_i. \quad (30)$$

Using the adjoint relation $\mathbf{q}_j^H \mathbf{K} = \lambda_j \mathbf{q}_j^H \mathbf{M}$ (a consequence of \mathbf{K} being Hermitian and the eigenvalue real) and the \mathbf{M} -orthogonality $\mathbf{q}_j^H \mathbf{M} \mathbf{q}_i = 0$ for $j \neq i$, Eq. (30) simplifies to

$$\mathbf{q}_j^H \mathbf{K}' \mathbf{q}_i + \lambda_j \mathbf{q}_j^H \mathbf{M} \mathbf{q}'_i = \lambda_i \mathbf{q}_j^H \mathbf{M} \mathbf{q}'_i, \quad (31)$$

Solving for $\mathbf{q}_j^H \mathbf{M} \mathbf{q}'_i$ gives the fundamental expression:

$$\mathbf{q}_j^H \mathbf{M} \mathbf{q}'_i = \frac{\mathbf{q}_j^H \mathbf{K}' \mathbf{q}_i}{\lambda_i - \lambda_j}, \quad j \neq i. \quad (32)$$

This formula, reproduced as Eq. (9) in the main text, reveals the inverse relationship between eigenvector sensitivity and the eigenvalue gap.

A.3 Expansion of the eigenvector derivative

Since the eigenvectors $\mathbf{q}_j(k)_{j=1}^n$ form an \mathbf{M} -orthonormal basis of \mathbb{C}^n , we can expand $\mathbf{q}'_i(k)$ in this basis:

$$\mathbf{q}'_i = \sum_{j=1}^n (\mathbf{q}_j^H \mathbf{M} \mathbf{q}'_i) \mathbf{q}_j. \quad (33)$$

Differentiating the normalization condition $\mathbf{q}_i^H \mathbf{M} \mathbf{q}_i = 1$ gives

$$\mathbf{q}_i^H \mathbf{M} \mathbf{q}'_i + (\mathbf{q}_i^H \mathbf{M} \mathbf{q}'_i)^H = 2\text{Re}(\mathbf{q}_i^H \mathbf{M} \mathbf{q}'_i) = 0, \quad (34)$$

so that $\text{Re}(\mathbf{q}_i^H \mathbf{M} \mathbf{q}'_i) = 0$; the imaginary part remains undetermined. This reflects the fact that the eigenvector's phase can be chosen arbitrarily as a function of k .

A.4 Phase convention and boundedness

To obtain a unique and convenient representation, we adopt a phase convention that eliminates the $j = i$ term in Eq. (33). By multiplying each eigenvector by a suitable k -dependent phase factor $e^{i\theta_i(k)}$ (which does not affect the eigenvalue or the MAC), we can enforce the stronger condition

$$\mathbf{q}_i^H \mathbf{M} \mathbf{q}'_i = 0. \quad (35)$$

This choice is always possible and preserves analyticity [48]. With Eq. (35), the $j = i$ term vanishes, and substituting Eq. (32) into Eq. (33) yields the explicit expansion

$$\mathbf{q}'_i = \sum_{j \neq i} \frac{\mathbf{q}_j^H \mathbf{K}' \mathbf{q}_i}{\lambda_i - \lambda_j} \mathbf{q}_j. \quad (36)$$

This is the complete derivation of Eq. (10) in the main text. From this expansion, the \mathbf{M} -norm of the derivative follows directly:

$$\|\mathbf{q}'_i\|_{\mathbf{M}}^2 = \mathbf{q}'_i{}^H \mathbf{M} \mathbf{q}'_i = \sum_{j \neq i} \frac{|\mathbf{q}_j^H \mathbf{K}' \mathbf{q}_i|^2}{(\lambda_i - \lambda_j)^2}, \quad (37)$$

where we have used the \mathbf{M} -orthonormality $\mathbf{q}_i^H \mathbf{M} \mathbf{q}_j = \delta_{ij}$. This establishes Eq. (11) in the main text and confirms that the derivative norm is finite under the simplicity assumption.

B Proof of Theorem 1 (Local Correct Tracking)

This appendix provides the complete rigorous proof of Theorem 1, establishing the existence of a sufficiently small step $\Delta k_{\max}(k)$ such that the correct tracking condition Eq. (19) holds.

B.1 Analytic expansion of the eigenvector

Under the analyticity and simplicity assumptions, the eigenvectors can be chosen as analytic functions of k [48]. Hence, for sufficiently small Δk , we have the Taylor expansion

$$\mathbf{q}_i(k + \Delta k) = \mathbf{q}_i(k) + \Delta k \mathbf{q}'_i(k) + \frac{(\Delta k)^2}{2} \mathbf{q}''_i(k) + O((\Delta k)^3). \quad (38)$$

B.2 Expansion of the self-MAC

Using the \mathbf{M} -orthonormality $\mathbf{q}_i^H(k) \mathbf{M} \mathbf{q}_j(k) = \delta_{ij}$ and the phase condition $\mathbf{q}_i^H(k) \mathbf{M} \mathbf{q}'_i(k) = 0$ (see Eq. (35)), we obtain from Eq. (38):

$$\mathbf{q}_i^H(k) \mathbf{M} \mathbf{q}_i(k + \Delta k) = \mathbf{q}_i^H(k) \mathbf{M} \mathbf{q}_i(k) + \Delta k \mathbf{q}_i^H(k) \mathbf{M} \mathbf{q}'_i(k) + \frac{(\Delta k)^2}{2} \mathbf{q}_i^H(k) \mathbf{M} \mathbf{q}''_i(k) + O((\Delta k)^3). \quad (39)$$

Differentiating the identity $\mathbf{q}_i^H \mathbf{M} \mathbf{q}'_i = 0$ gives

$$\mathbf{q}_i^H(k) \mathbf{M} \mathbf{q}''_i(k) = -\mathbf{q}_i^H(k) \mathbf{M} \mathbf{q}'_i(k) = -\|\mathbf{q}'_i(k)\|_{\mathbf{M}}^2, \quad (40)$$

where $\|\mathbf{v}\|_{\mathbf{M}}^2 := \mathbf{v}^H \mathbf{M} \mathbf{v}$. Substituting into Eq. (39) yields

$$\mathbf{q}_i^H(k) \mathbf{M} \mathbf{q}_i(k + \Delta k) = 1 - \frac{(\Delta k)^2}{2} \|\mathbf{q}'_i(k)\|_{\mathbf{M}}^2 + O((\Delta k)^3), \quad (41)$$

Taking the squared modulus and using $|1 - a|^2 = 1 - 2a + O(a^2)$ with $a = \frac{(\Delta k)^2}{2} \|\mathbf{q}'_i(k)\|_{\mathbf{M}}^2$, we obtain

$$\begin{aligned} \text{MAC}[\mathbf{q}_i(k), \mathbf{q}_i(k + \Delta k)] &= \left| 1 - \frac{(\Delta k)^2}{2} \|\mathbf{q}'_i(k)\|_{\mathbf{M}}^2 + O((\Delta k)^3) \right|^2 \\ &= 1 - (\Delta k)^2 \|\mathbf{q}'_i(k)\|_{\mathbf{M}}^2 + O((\Delta k)^3). \end{aligned} \quad (42)$$

B.3 Expansion of the cross-MAC

For $j \neq i$, we again use Eq. (38) and the orthogonality $\mathbf{q}_i^H \mathbf{M} \mathbf{q}_j = 0$:

$$\begin{aligned} \mathbf{q}_i^H(k) \mathbf{M} \mathbf{q}_j(k + \Delta k) &= \mathbf{q}_i^H(k) \mathbf{M} \mathbf{q}_j(k) + \Delta k \mathbf{q}_i^H(k) \mathbf{M} \mathbf{q}'_j(k) + O((\Delta k)^2) \\ &= \Delta k \frac{\mathbf{q}_i^H \mathbf{K}' \mathbf{q}_j}{\lambda_j - \lambda_i} + O((\Delta k)^2), \end{aligned} \quad (43)$$

In the last equality we have employed the projection formula Eq. (9) with the roles of i and j interchanged. Define the (finite) coupling coefficient

$$c_{ij}(k) = \frac{\mathbf{q}_i^H(k) \mathbf{K}'(k) \mathbf{q}_j(k)}{\lambda_j(k) - \lambda_i(k)}. \quad (44)$$

Then Eq. (43) becomes $\mathbf{q}_i^H \mathbf{M} \mathbf{q}_j(k + \Delta k) = \Delta k c_{ij}(k) + O((\Delta k)^2)$, and consequently

$$\text{MAC}[\mathbf{q}_i(k), \mathbf{q}_j(k + \Delta k)] = |\Delta k c_{ij}(k) + O((\Delta k)^2)|^2 = (\Delta k)^2 |c_{ij}(k)|^2 + O((\Delta k)^3). \quad (45)$$

B.4 Local estimates

From the asymptotic expressions Eq. (42) and Eq. (45), we can choose a $\delta_0 > 0$ (depending on k) and constants C_1 and C_2 (depending on $|\mathbf{q}'_i(k)|$ and $\max_{j \neq i} |c_{ij}(k)|$) such that for all $0 < \Delta k \leq \delta_0$ and all $j \neq i$,

$$\text{MAC}[\mathbf{q}_i(k), \mathbf{q}_i(k + \Delta k)] \geq 1 - C_1(\Delta k)^2, \quad \text{MAC}[\mathbf{q}_i(k), \mathbf{q}_j(k + \Delta k)] \leq C_2(\Delta k)^2. \quad (46)$$

For instance, one may take $C_1 = 2|\mathbf{q}'_i(k)|^2$ and $C_2 = 2 \max_{j \neq i} |c_{ij}(k)|^2$, and choose δ_0 sufficiently small so that the remainders in Eq. (42) and Eq. (45) are bounded by $|\mathbf{q}'_i(k)|^2(\Delta k)^2$ and $\max |c_{ij}|^2(\Delta k)^2$, respectively.

B.5 Construction of $\Delta k_{\max}(k)$

Define

$$\Delta k_{\max}(k) := \min \left(\delta_0, \frac{1}{\sqrt{C_1 + C_2}} \right). \quad (47)$$

Then for any $0 < \Delta k \leq \Delta k_{\max}(k)$, we have $(\Delta k)^2 \leq 1/(C_1 + C_2)$, which implies $1 - C_1(\Delta k)^2 \geq C_2(\Delta k)^2$. Combining this with Eq. (46) yields

$$\text{MAC}[\mathbf{q}_i(k), \mathbf{q}_i(k + \Delta k)] \geq 1 - C_1(\Delta k)^2 \geq C_2(\Delta k)^2 \geq \text{MAC}[\mathbf{q}_i(k), \mathbf{q}_j(k + \Delta k)], \quad (48)$$

and in fact the first inequality is strict for $\Delta k > 0$ (because $1 - C_1(\Delta k)^2 > C_2(\Delta k)^2$). Hence Eq. (19) holds for every $j \neq i$.

CRedit authorship contribution statement

Dong Xiao: Conceptualization, Methodology, Software, Data curation, Formal analysis, Writing - Original draft preparation, Writing - Review Editing, Visualization. **Zahra Sharif-Khodaie:** Supervision, Writing - Review Editing. **M. H. Aliabadi:** Supervision, Writing - Review Editing.

Declaration of competing interest

The authors declare that they have no known competing financial interests or personal relationships that could have appeared to influence the work reported in this paper.

Acknowledgements

The first author acknowledges the financial support from the K. C. Wong Postdoctoral Fellowship, funded by the K. C. Wong Education Foundation.

Data availability

The source code and data supporting this study will be made publicly available upon publication at <https://github.com/dongxiao96/DisperPy>. This Python-based tool implements the proposed adaptive wavenumber sampling algorithm, and the repository contains Jupyter notebooks that reproduce

all numerical examples presented in this paper. A graphical user interface (GUI) is under development to further lower the barrier for users.

References

- [1] Joseph L. Rose. *Ultrasonic Guided Waves in Solid Media*. Cambridge University Press, Cambridge, 2014.
- [2] Victor Giurgiutiu. *Structural Health Monitoring with Piezoelectric Wafer Active Sensors*. Elsevier, June 2014.
- [3] M H Ferri Aliabadi and Z Sharif Khodaei. *Structural Health Monitoring for Advanced Composite Structures*, volume 08 of *Computational and Experimental Methods in Structures*. World Scientific (Europe), February 2018.
- [4] Dong Xiao, Zahra Sharif-Khodaei, and M. H. Aliabadi. Hybrid physics-based and data-driven impact localisation for composite laminates. *International Journal of Mechanical Sciences*, 274:109222, July 2024.
- [5] Dong Xiao, Francisco de Sá Rodrigues, Zahra Sharif-Khodaei, and M. H. Aliabadi. A general probabilistic framework for impact localisation based on flexural wave propagation. *Mechanical Systems and Signal Processing*, 226:112320, March 2025.
- [6] Mariusz Kaczmarek, Bogdan Piwakowski, and Radosław Drelich. Noncontact Ultrasonic Nondestructive Techniques: State of the Art and Their Use in Civil Engineering. *Journal of Infrastructure Systems*, 23(1):B4016003, March 2017.
- [7] Pascal Laugier and Guillaume Haïat. *Bone Quantitative Ultrasound*. SpringerLink Bücher. Springer Science+Business media B.V, Dordrecht, 2011.
- [8] M.J.S. Lowe. Matrix techniques for modeling ultrasonic waves in multilayered media. *IEEE Transactions on Ultrasonics, Ferroelectrics, and Frequency Control*, 42(4):525–542, July 1995.
- [9] Ameneh Maghsoodi, Abdolreza Ohadi, and Mojtaba Sadighi. Calculation of Wave Dispersion Curves in Multilayered Composite-Metal Plates. *Shock and Vibration*, 2014(1):410514, 2014.
- [10] S. I. Rokhlin and L. Wang. Stable recursive algorithm for elastic wave propagation in layered anisotropic media: Stiffness matrix method. *The Journal of the Acoustical Society of America*, 112(3):822–834, September 2002.
- [11] Armin Huber. Stiffness matrix method for modeling of guided waves in multilayered anisotropic plates: the dispersion calculator. Überherrn, Deutschland, July 2024.
- [12] F. Hernando Quintanilla, Z. Fan, M. J. S. Lowe, and R. V. Craster. Guided waves’ dispersion curves in anisotropic viscoelastic single- and multi-layered media. *Proceedings of the Royal Society A: Mathematical, Physical and Engineering Sciences*, 471(2183):20150268, November 2015.
- [13] A. T. I. Adamou and R. V. Craster. Spectral methods for modelling guided waves in elastic media. *The Journal of the Acoustical Society of America*, 116(3):1524–1535, September 2004.
- [14] Mohammed Aslam, Junpil Park, and Jaesun Lee. A comprehensive study on guided wave dispersion in complex structures. *International Journal of Mechanical Sciences*, 269:109089, May 2024.
- [15] Ivan Bartoli, Alessandro Marzani, Francesco Lanza Di Scalea, and Erasmo Viola. Modeling wave propagation in damped waveguides of arbitrary cross-section. *Journal of Sound and Vibration*, 295(3-5):685–707, August 2006.
- [16] Alessandro Marzani, Erasmo Viola, Ivan Bartoli, Francesco Lanza Di Scalea, and Piervincenzo Rizzo. A semi-analytical finite element formulation for modeling stress wave propagation in axisymmetric damped waveguides. *Journal of Sound and Vibration*, 318(3):488–505, December 2008.
- [17] Michel Castaings and Michael Lowe. Finite element model for waves guided along solid systems of arbitrary section coupled to infinite solid media. *The Journal of the Acoustical Society of America*, 123(2):696–708, February 2008.

- [18] Wenbo Duan and Tat-Hean Gan. Investigation of guided wave properties of anisotropic composite laminates using a semi-analytical finite element method. *Composites Part B: Engineering*, 173:106898, September 2019.
- [19] Takahiro Hayashi, Won-Joon Song, and Joseph L Rose. Guided wave dispersion curves for a bar with an arbitrary cross-section, a rod and rail example. *Ultrasonics*, 41(3):175–183, May 2003.
- [20] Vu-Hieu Nguyen and Salah Naili. Ultrasonic wave propagation in viscoelastic cortical bone plate coupled with fluids: a spectral finite element study. *Computer Methods in Biomechanics and Biomedical Engineering*, 16(9):963–974, September 2013.
- [21] Daniel H. Cortes, Subhendu K. Datta, and Osama M. Mukdadi. Dispersion of elastic guided waves in piezoelectric infinite plates with inversion layers. *International Journal of Solids and Structures*, 45(18):5088–5102, September 2008.
- [22] J E Quiroga, L Mujica, R Villamizar, M Ruiz, and J Camacho. Estimation of dispersion curves by combining Effective Elastic Constants and SAFE Method: A case study in a plate under stress. *Journal of Physics: Conference Series*, 842(1):012069, May 2017.
- [23] M. Mazzotti, A. Marzani, I. Bartoli, and E. Viola. Guided waves dispersion analysis for prestressed viscoelastic waveguides by means of the SAFE method. *International Journal of Solids and Structures*, 49(18):2359–2372, September 2012.
- [24] Namita Nanda and Santosh Kapuria. A semi-analytical spectral element method for dispersion analysis of guided waves in functionally graded plates. *Acta Mechanica*, December 2025.
- [25] Brian Pavlakovic, Mike Lowe, David Alleyne, and Peter Cawley. Disperse: A General Purpose Program for Creating Dispersion Curves. In Donald O. Thompson and Dale E. Chimenti, editors, *Review of Progress in Quantitative Nondestructive Evaluation: Volume 16A*, pages 185–192. Springer US, Boston, MA, 1997.
- [26] Armin Huber. The Dispersion Calculator: A Free Software for Calculating Dispersion Curves of Guided Waves. In *20th World Conference on Non-Destructive Testing (WCNDT 2024)*, volume 29, pages 1–17, Incheon, Südkorea, May 2024. NDT.net. Number: 6.
- [27] Menglong Liu, Wenyan Zhang, Xiao Chen, Lun Li, Kai Wang, Hong Wang, Fangsen Cui, and Zhongqing Su. Modelling guided waves in acoustoelastic and complex waveguides: From SAFE theory to an open-source tool. *Ultrasonics*, 136:107144, January 2024.
- [28] Paolo Bocchini, Alessandro Marzani, and Erasmo Viola. Graphical User Interface for Guided Acoustic Waves. *Journal of Computing in Civil Engineering*, 25(3):202–210, May 2011.
- [29] Adil Han Orta, Mathias Kersemans, and Koen Van Den Abeele. A comparative study for calculating dispersion curves in viscoelastic multi-layered plates. *Composite Structures*, 294:115779, August 2022.
- [30] Jabid E. Quiroga, Octavio A. González-Estrada, and Miguel Díaz-Rodríguez. Evaluation of Numerical Methods for Dispersion Curve Estimation in Viscoelastic Plates. *Eng*, 6(9):240, September 2025.
- [31] Darun Barazanchy and Victor Giurgiutiu. A comparative convergence and accuracy study of composite guided-ultrasonic wave solution methods: Comparing the unified analytic method, SAFE method and DISPERSE. *Proceedings of the Institution of Mechanical Engineers, Part C: Journal of Mechanical Engineering Science*, 231(16):2961–2973, August 2017.
- [32] R. Allemang and David L. Brown. A correlation coefficient for modal vector analysis. In *Proceedings of the 1st International Modal Analysis Conference (1st IMAC)*, pages 110–116, Orlando, 1982.
- [33] Tshilidzi Marwala. *Finite-element-model Updating Using Computational Intelligence Techniques*. Springer London, London, 2010.
- [34] M J Desforges, J E Cooper, and J R Wright. Mode Tracking During Flutter Testing Using the Modal Assurance Criterion. *Proceedings of the Institution of Mechanical Engineers, Part G: Journal of Aerospace Engineering*, 210(1):27–37, January 1996.
- [35] N. C. Perkins and C. D. Mote. Comments on curve veering in eigenvalue problems. *Journal of Sound and Vibration*, 106(3):451–463, May 1986.
- [36] John Von Neumann and Eugene Wigner. No crossing rule. *Physik*, 30:467–470, 1929.

- [37] Arthur W. Leissa. On a curve veering aberration. *Zeitschrift für angewandte Mathematik und Physik ZAMP*, 25(1):99–111, January 1974.
- [38] Hauke Gravenkamp, Bor Plestenjak, and Daniel A. Kiefer. Notes on osculations and mode tracing in semi-analytical waveguide modeling. *Ultrasonics*, 135:107112, December 2023.
- [39] T. Uzer, D. W. Noid, and R. A. Marcus. Uniform semiclassical theory of avoided crossings. *The Journal of Chemical Physics*, 79(9):4412–4425, November 1983.
- [40] Michal Masek, Miloslav Capek, Lukas Jelinek, and Kurt Schab. Modal Tracking Based on Group Theory. *IEEE Transactions on Antennas and Propagation*, 68(2):927–937, February 2020.
- [41] Xu Zhang, Lei Chen, Gang Liu, Zehui Zhang, and Jiachen Wang. An improved modal tracking algorithm for dispersion analysis of arbitrary prestressed plates. *Thin-Walled Structures*, 205:112582, December 2024.
- [42] Taizo Maruyama and Kazuyuki Nakahata. Continuation Approach Combined with Semi-Analytical Finite-Element Method for Solving Guided-Wave Dispersion Equation. *Journal of Nondestructive Evaluation*, 44, May 2025.
- [43] Xudong Yu, Bohan Liu, Hai Shen, Peng Zuo, and Zheng Fan. Automatic mode tracing of dispersion relations for guided waves in elastic waveguides via physics-driven affinity propagation (AP) clustering. *Mechanical Systems and Signal Processing*, 222:111746, January 2025.
- [44] Gregory J. Hatton. The noncrossing rule and spurious avoided crossings. *Physical Review A*, 14(3):901–910, September 1976.
- [45] C. Alden Mead. The "noncrossing" rule for electronic potential energy surfaces: The role of time-reversal invariance. *The Journal of Chemical Physics*, 70(5):2276–2283, March 1979.
- [46] Miroslav Pastor, Michal Binda, and Tomáš Harčarik. Modal Assurance Criterion. *Procedia Engineering*, 48:543–548, January 2012.
- [47] H. W. Kuhn. The Hungarian method for the assignment problem. *Naval Research Logistics Quarterly*, 2(1-2):83–97, 1955.
- [48] Tosio Kato. *Perturbation Theory for Linear Operators*, volume 132 of *Classics in Mathematics*. Springer Berlin Heidelberg, Berlin, Heidelberg, 1995.
- [49] Jing Mu and Joseph L. Rose. Guided wave normal modes in hollow cylinders with viscoelastic coatings. *AIP Conference Proceedings*, 975(1):86–91, February 2008.